Convective-scale variations in the inner-core rainbands of a tropical cyclone

Submitted for publication in *Journal of the Atmospheric Sciences*
May 2012
Revised
August 2012

Anthony C. Didlake, Jr., and Robert A. Houze, Jr.
University of Washington, Seattle, Washington

Corresponding author: Anthony C. Didlake, Jr., Department of Atmospheric Sciences
University of Washington, Box 351640, Seattle, WA 98195
E-mail address: didlake@washington.edu

Abstract

Airborne Doppler radar documented a variety of convective-scale structures within the inner-core rainbands of Hurricane Rita (2005). As predicted by past studies, wind shear determined azimuthal variations in the convection. All convective-scale circulations had radial inflow at low levels, upward motion, and outflow in the mid-troposphere. Convective cells at smaller radii contained a low-level tangential jet determined largely by tangential acceleration due to angular momentum conservation (uv/r term), while cells at larger radii contained a low-level and/or midlevel jet determined jointly by the uv/r and vertical advection terms. The outflow was at a higher (lower) altitude for the outer (inner) cells.

Radial variations in the convective cells are attributable to differences in buoyancy and vertical shear of the radial wind ($\partial u/\partial z$). More buoyant updrafts at larger radii enhance vertical advection of v, creating local tangential jets at midlevels. At smaller radii, the stronger low-level radial inflow contributes to a greater $\partial u/\partial z$, confining convectively generated jets to low levels. The low-level tangential jet and convectively generated pressure gradients produce outward-pointing supergradient acceleration that decelerates the boundary layer inflow. Consequently, this supergradient flow will enhance convergence and convection at the radius of inner rainband cells, increasing the likelihood of secondary eyewall formation. It is hypothesized that a critical zone for secondary eyewall formation exists where sufficiently high $\partial u/\partial z$ consistently constrains the altitudes of convectively generated supergradient flow so that convection in this radial zone leads to a newly developed eyewall. Once an incipient secondary eyewall forms at a certain radius, subsidence occurring along its inner edge separates it from the primary eyewall.

1. Introduction

Improving intensity forecasts of tropical cyclones almost certainly requires a better understanding of the structure and dynamics of the storm's inner core (the region within ~200 km of the storm center). Inner-core convection, which populates the region outside of the eyewall, can play a determining role in the storm's intensity either by modifying dynamics on the vortex scale, or by modifying the boundary layer air that feeds into the eyewall (e.g. Montgomery and Kallenbach 1997; Barnes et al. 1983; Powell 1990b). However, the exact role of the inner-core convection remains uncertain and difficult to assess since the inner core's evolution involves a complex interaction among processes occurring on scales differing by many orders of magnitude (Marks and Shay 1998).

Despite these uncertainties, observations show that much of the inner-core convection is organized into a system of spiral rainbands termed the stationary band complex (SBC) since the complex remains pseudo-stationary relative to the translating storm center (Willoughby et al. 1984). Houze (2010) has presented an updated conceptual model of this family of rainbands seen in tropical cyclones. The principal rainband is the most prominent member of the family, and it contains discrete or connected convective cells in its upwind portion and predominantly stratiform precipitation in its downwind end. The principal rainband, often regarded as an effective boundary between vortex-scale and environmental processes, contains intense updrafts that build a midlevel tangential wind jet and two distinct downdrafts that bring low moist static energy air into the boundary layer inflow (Barnes et al. 1983; Powell 1990a,b; Hence and Houze 2008; Didlake and Houze 2009). Smaller, secondary rainbands form radially inward of the principal band and typically contain weaker and more transient convection. Some secondary bands have been attributed to convectively coupled vortex-Rossby waves, which propagate

azimuthally and radially outward from the eyewall (Montgomery and Kallenbach 1997; Corbosiero et al. 2006). According to Willoughby et al. (1984), a connecting band may join the downwind end of the principal band to the eyewall and contains either weak convective or stratiform precipitation.

The structure of inner-core convective elements embedded in the various mesoscale rainbands of the SBC varies significantly with respect to both radius and azimuth relative to the storm center. Using satellite radar reflectivity data, Hence and Houze (2012) found that at smaller radii convective cells are shallower, possibly because of vertical confinement by the eyewall outflow. Their findings are also consistent with studies showing that convective available potential energy (CAPE) decreases with decreasing radius (e.g. Frank 1977; Bogner et al. 2000; Eastin et al. 2005); however, increased entrainment, owing to increased shear of the vortex wind, may also play a larger role in suppressing convective cell development at smaller radii. Using linear theory and nonlinear model simulations of a steady-state storm, Kepert (2001) and Kepert and Wang (2001) demonstrated that the boundary layer, regarded as the frictional response to the cyclone structure in the free atmosphere, becomes shallower with decreasing radius. This variation in the inner-core boundary layer depth has been verified by observations in numerous storms (Kepert 2006a,b; Schwendike and Kepert 2008; Zhang et al. 2011) and is another factor that may relate to the variation of convective-scale structures relative to distance from the storm center.

The dominant azimuthal variations observed in the inner-core regions of tropical cyclones are wavenumber-1 asymmetries generated by storm motion and vertical wind shear. The storm motion introduces an asymmetry into the wind field, which shifts inner-core convection located outside of the eyewall to the front-right quadrant of the storm (Frank 1984;

Burpee and Black 1989; Lonfat et al. 2004). The effect of storm motion is apparent only when the wind shear is weak (<5 m s^{-1}), as stronger wind shear has an overriding influence on the storm's asymmetry (Chen et al. 2006; Corbosiero and Molinari 2003). The presence of significant wind shear tends to shift the most robust inner-core convection into the storm's downshear half. Subsequently, stratiform precipitation tends to occupy the regions left of the wind shear (Corbosiero and Molinari 2002, 2003; Hence and Houze 2012).

Past studies such as Willoughby et al. (1984) and Houze (2010) provide insight into the distribution of mesoscale features in the inner core outside of the eyewall; however, a detailed understanding of the associated embedded convective-scale elements has not been attained. Yet the convective-scale entities within the rainbands are the loci of active vertical exchanges impacting the storm dynamics. The current study will address this knowledge gap by analyzing high-resolution aircraft observations of inner-core convection from Hurricane Rita collected during the 2005 Hurricane Rainband and Intensity Change Experiment (RAINEX; Houze et al. 2006, 2007). The dataset obtained in RAINEX with the National Center for Atmospheric Research (NCAR) Electra Doppler Radar (ELDORA) is ideally suited to address this problem. The ELDORA has a unique combination of high spatial resolution and rapid sampling rate that allowed detailed documentation of the convective-scale structures, and flights were conducted in a variety of locations within the inner-core regions of storms. In this study, we do not emphasize the location of convective cells relative to the different types of rainbands in the SBC, but rather we examine the variability of the convection according to its location relative to the storm center and environmental shear vector, regardless of its parent rainband. This approach is practical because the location of the storm center is always known, whereas the classification of rainbands is somewhat subjective.

Section 2 describes the data and methods of analysis. Section 3 examines the reflectivity pattern of the inner core. Section 4 investigates the radial variability of the convection, while Section 5 investigates its azimuthal variability. Section 6 discusses the implications that the results have on secondary eyewall formation. Finally, Section 7 presents the conclusions of the study.

2. Data and Methodology

a. Instrumentation and data synthesis

On 21 September 2005, the Naval Research Laboratory (NRL) P3 aircraft, equipped with the NCAR ELDORA instrument, was deployed in RAINEX to investigate the inner core of Hurricane Rita. The data used for this study were observed during 1845-2032 UTC. ELDORA is an X-band dual-Doppler radar noted for its high sampling resolution. It operates with two beams pointing approximately 16° fore and aft, such that the beams intersect at 400-m intervals as the aircraft flies along a track [for more on ELDORA, see Hildebrand et al. (1996)]. Because of the speed of the aircraft, the two independent radar scans are essentially coincident in time at each beam crossing, thus providing two components of the wind vector everywhere within range of the radar. The radar data were first corrected for navigation and instrumental errors (Testud et al. 1995; Bosart et al. 2002) and manually edited using the NCAR Solo II software (Oye et al. 1995) to remove noise and radar artifacts. The reflectivity and velocity data were then interpolated to a Cartesian grid with a resolution of 600 m in the horizontal and 400 m in the vertical. The lowest vertical level of data was 800 m, as sea spray contaminates the current radar observations below this level.

The radar data collected during 1845-1927 UTC were divided into multiple sections to avoid sharp turns in the flight track and to keep the dual-Doppler calculations within practical limitations of computer memory. Figure 1 shows the resulting sections A-D in relation to the 2-km level reflectivity pattern. In this paper, sections A and B will be considered the upwind end, and sections C and D will be considered the downwind end. The three-dimensional wind field was retrieved using two different dual-Doppler synthesis methods. The first method is a variational technique that minimizes the differences between radar-measured and retrieved velocity components while approximately adhering to anelastic mass continuity and vertical velocity boundary conditions (a complete description is given in Reasor et al. 2009). The second method involves interpolation of the horizontal wind components with the REORDER software (Oye and Case 1994), then solving for the vertical wind with the Cartesian Editing and Display of Radar data under Interactive Control (CEDRIC; Mohr et al. 1986) software (further description is given in Hence and Houze 2008). The storm translation was assumed to be constant and was removed from the wind field. A two-step three-dimensional Leise filter was then applied, yielding a minimum resolvable wavelength of approximately 5 km. The two synthesis methods yielded velocity magnitudes that were generally within 5 m s^{-1} of each other while their qualitative patterns remained similar throughout most of the domain. Notable differences between the two methods occurred in altitudes below the 2 km level. The analyses presented herein are from the REORDER/CEDRIC technique, which retrieved low-level wind fields that were most consistent with concurrent dropsonde observations. This technique chooses the larger reflectivity value of the fore and aft scans at each pixel, which extends the length of some robust cells in the final reflectivity field by up to 3 km. The dropsondes used in this study were released from the NRL and National Oceanic and Atmospheric Administration (NOAA) P3

aircraft during the time span 1748-1908 UTC. These dropsonde data were quality controlled with either the NCAR Aspen or NOAA Hurricane Research Division (HRD) Editsonde software.

After the wind field was retrieved, the data were initially examined using the NCAR Zebra analysis and visualization software (originally designed by Corbet et al. 1994, later modified by James et al. 2000, and presently maintained at the University of Washington), which interactively plots overlays of multiple parameters from horizontal and vertical cross sections of the dataset. We then interpolated the data to a cylindrical coordinate system with radial resolution of 600 m and azimuthal resolution of 0.375°. The vortex centers used for this interpolation follow the storm track determined by Bell et al. (2012). For their analyzed track of Rita, a cubic spline fit was implemented on vortex centers that maximize the radar-observed tangential wind within a 3-km-wide annulus centered on the radius of maximum wind (Marks et al. 1992). At times when sufficient radar data were not available, aircraft center fixes were used. The results shown in this paper are not sensitive to small variations in the analyzed circulation centers.

b. Data separation techniques

Regions of convective precipitation are generally seen on radar as locally vertically oriented cells of high reflectivity, while regions of stratiform precipitation are generally weaker, less variable in the horizontal, and often signaled by a reflectivity bright band near the melting level (Houze 1997). To separate the convective and stratiform precipitation in Rita's inner core, we use the convective/stratiform separation technique developed by Churchill and Houze (1984), Steiner et al. (1995), and Yuter and Houze (1997). This technique searches for the distinguishing convective radar signatures by comparing the 2-km reflectivity at each pixel with the reflectivity average of the surrounding area. If this difference in reflectivity exceeds a certain threshold, then

this pixel along with the surrounding pixels within a reflectivity-weighted radius are deemed convective regions. Pixels with a reflectivity value exceeding 42 dBZ are automatically deemed convective. The remaining pixels with sufficient reflectivity values are classified as stratiform. Further details of this technique can be found in appendix A of Didlake and Houze (2009). The results of the separation algorithm are presented in Fig. 2.

To analyze the convection's variability with radius, the data were divided into "inner" and "outer" regions relative to the spiral shown in Fig. 2. The cylindrical coordinate equation for the spiral shown is $r = 49 \cdot 2^{(2\pi/\theta)}$, where r is the radius in km and θ is the angle in radians starting at $\theta = \pi$ (due west). This spiral was chosen to follow the lane of weak precipitation extending from section A through the middle of section C. Since this study will not focus on eyewall convection, the radar data within 45 km from the center were excluded from the inner region.

c. Hurricane Rita

Rita began as a tropical depression near the Bahamas on 18 September 2005 and intensified to a hurricane on 20 September as it tracked west toward the Gulf of Mexico. Over the next 36 h, Rita intensified rapidly into a category 5 (Saffir 2003) storm. At 1800 UTC 21 September, Rita had maximum sustained winds of 75 m s^{-1} and a central pressure of 920 hPa. The storm was traveling toward the west at 6 m s^{-1}. Just hours after the aircraft mission was completed, Rita reached its maximum intensity (peak wind 80 m s^{-1} and minimum pressure 895 hPa), becoming one of the strongest storms recorded in the Atlantic Basin (Beven et al. 2008). Further descriptions of the RAINEX observations and model simulation of Rita can be found in Houze et al. (2006, 2007).

3. Variation of the reflectivity field

The reflectivity field shown in Fig. 1 exhibits significant radial and azimuthal variation, which is also captured in the convective/stratiform separation seen in Fig. 2. For both inner and outer regions, the azimuthal variation generally reflects the changing thermodynamic structure and differential advection of hydrometeors along the rainbands. Convection in the inner region of sections A and B appears to be broken into two spiral bands containing convective cells embedded in stratiform precipitation, while in section C the convective cells appear clustered together. The outer region contains intense convection organized as isolated cells in section A and organized as a nearly continuous band in section B. These upwind portions have sufficient conditional instability to support convective cell growth, but this instability depletes as air travels downwind along the rainbands. Slowly falling ice particles produced by these convective cells are continuously advected downwind. As a result, downwind sections of the rainband become increasingly dominated by stratiform precipitation in both inner and outer regions. This progression along the rainband from convective structure upwind to stratiform downwind is well known, having been first documented by Atlas et al. (1963).

The orientation of the reflectivity field agrees well with observational composite studies of the wind shear's impact on convection asymmetry. Following the method of Hence and Houze (2011, 2012), we calculated the 850-200 hPa environmental wind shear from the National Center for Environmental Prediction (NCEP) reanalysis winds in a radial ring of 500-750 km from the storm center. For the case considered here, this shear vector was pointing east (89.5°) with a magnitude of 10 m s^{-1}. Corbosiero and Molinari (2002, 2003) examined the orientation of lightning strikes in tropical cyclones relative to the wind shear and storm motion. Under medium wind shear (5-10 m s^{-1}), they found lightning strike maxima in the downshear right quadrant for

the “outer rainband” region (corresponds to our outer region) and in the downshear left quadrant for the “inner-core” region (corresponds to our inner region). Consistent with these findings, the most clustered active convection in our observations was located in outer section B (downshear right) and inner section C (downshear left). Hence and Houze (2012) examined three-dimensional reflectivity data from the Tropical Rainfall Measurement Mission (TRMM) satellite’s Precipitation Radar and found convective structures as a function of storm sector relative to the shear to be consistent with Corbosiero and Molinari’s (2002, 2003) lightning analysis. They further found that stratiform precipitation was most prevalent in the downshear left quadrant. From the regions sampled by ELDORA in this study, it was clear that stratiform rain was most widespread in sections C and D, which inhabit the downshear left quadrant. Additional observations (presented in a future study) indicate that the stratiform rain is also prevalent in the upshear left quadrant of the rainband complex. Given these results, we suggest that shear was the factor most responsible for determining the azimuthal variation of Rita’s rainband convection.

4. Convective cells in the inner and outer upwind regions

a. Composite characteristics

Hence and Houze (2008) examined the convection in Rita’s outer upwind region and determined that these cells were of the “principal rainband” type, exhibiting reflectivity and kinematic characteristics observed in other major tropical cyclone rainbands (Barnes et al. 1983; Powell 1990a). Individual cross sections of the most robust cells highlighted the presence of a midlevel tangential wind jet, an overturning updraft circulation, a low-level downdraft and an inner-edge downdraft (Didlake and Houze 2009) emanating from upper levels. In this section

and the next section, a composite approach will be used to analyze the entire volume of upwind convective precipitation to determine the consistency of these characteristics in the outer region and to compare with the characteristics of active convection in the inner region.

Cross section composites were attained using the following procedure. For every radial swath within the cylindrical coordinate system (occurring at azimuthal intervals of 0.375°), locations of convectively classified areas (Fig. 2) in sections A and B were identified. For each individual radial swath, the innermost convectively classified pixel marked the anchor for the cross section. A cross section was taken along this radial swath that extended 12 km radially inward of the anchor and 36 km radially outward to incorporate all characteristics associated with an individual convective cell. Only cross sections that contained a convectively classified region at least 8 km in radial length were included in the composites. If an individual radial swath contained additional occurrences of 8-km-long convective regions beyond the innermost convective region, then cross sections of these regions were also taken and included in the analysis. The anchor locations determined whether the cross section lay in the inner or outer region. The inner region composite comprised 284 cross sections and the outer region comprised 263 cross sections.

Figures 3 and 4 show the composite fields of wind (radial, tangential, and vertical components) and reflectivity. As is evident in the reflectivity plan view, the reflectivity of the composite outer cell is more intense than the inner cell. Deep radial inflow feeds into the convective cells in both the inner and outer regions (Figs. 3a, 4a). Dropsonde measurements (not shown) confirm these inflow depths, which are slightly greater than the axisymmetric boundary layer inflow depths determined by Zhang et al. (2011) at the corresponding radii. Still, the current observations are typical of the inflow depths associated with active convection in the

rainband region (Barnes et al. 1983; Barnes and Powell 1995). These convective cells, which occur at distances between 2-5 times the radius of maximum wind, have inflow magnitudes that are consistent with the Doppler radar composites from Rogers et al. (2012). The inner cell has stronger inflow that decreases rapidly with height and turns into outflow with a maximum at 6 km altitude. The inflow for the outer cell has a more gradual decrease with height and the outflow layer is positioned higher at 7.5 km altitude. For both regions, the outflow magnitude is significantly enhanced near the radius of the reflectivity tower, suggesting that the convective cells are directly influencing the outflow layer.

Convective cells in both regions contain local maxima in tangential wind (Figs. 3b, 4b). For the inner convective cell, the tangential jet is located near 1 km altitude and the winds above decline rapidly with height. For the outer convective cell, the main tangential jet occurs at the 2 km level and a strand of elevated winds trails off at the 5 km level along the outer side of the cell. Figure 5 highlights the magnitudes, altitudes, and frequencies of the tangential jets occurring in the convective cells. In the inner cells, tangential jets are found at all levels between 0.8 and 3.6 km altitude. The vast majority of tangential jets occur at 0.8 km altitude, which is consistent with the composite maximum in Fig. 3b. The rainband studied by Barnes and Stossmeister (1986), which occurred at radial distances comparable to the inner convective cells, also exhibited a similarly low-level tangential jet throughout its lifetime. For the outer cells, the greatest frequency of jets occurs at 2 km altitude, which is consistent with the composite maximum in Fig. 4b; however, jets of comparable magnitudes occur anywhere up to 9 km altitude. Outer convective cells regularly exhibit these elevated tangential jets, as observed in the current dataset and in other storms from previous studies (Barnes et al. 1983; Samsury and Zipser 1995; Hence and Houze 2008). In comparing the inner and outer regions, the outer cells

are capable of producing tangential jets in both the low and midlevels, while the inner cells produce a singular jet that is confined to a lower altitude.

The vertical velocity composites (Figs. 3c, 4c) show the updrafts associated with the convective cells. The average updraft in the inner region is tilted outward along the inner side of the reflectivity tower, while the outer region updraft is more erect and centrally positioned within the cell. Figure 6 further demonstrates the differences between the two cells; it shows a profile of the average vertical velocities in the convective regions. The average vertical velocity is upward motion that peaks near 5 km altitude for the inner cells and 6 km altitude for the outer cells. Outer cells contain stronger updrafts and downdrafts through the depth of the rainband convection. Although not apparent in Fig. 4c, outer cell downdrafts, with magnitudes > 2 m s^{-1}, occur near 8 km altitude (Fig. 6). Individual cross sections confirm these results, with occurrences of inner-edge downdrafts originating from midlevel outflow and descending to the surface, likely producing the sharp inner-edge reflectivity gradient and lane of weak precipitation between the inner and outer regions.

Figures 3d and 4d show the divergence patterns of the convective cells as well as selected streamlines of the overturning secondary circulation. Both cells contain convergence maxima in the low levels, but these maxima occur in different vertical locations relative to their corresponding tangential wind maxima. The inner-cell convergence maximum occurs near 2.5 km altitude, which is above the tangential wind maximum (Fig. 3b), while the outer cell convergence maximum occurs near 1.5 km altitude, which is below the tangential wind maximum (Fig. 4b). In an analysis of tropical cyclone boundary layer heights, Zhang et al. (2011) noted that the top of the mixed layer (defined as the layer of nearly constant virtual potential temperature) consistently remains below the height of the maximum wind speed. Given

this organization of the boundary layer, the converging air that initiates the outer cell updraft is more likely to have a higher moist static energy than the converging air in the inner cell. Furthermore, the thermodynamics of tropical cyclones exhibit decreasing average CAPE with decreasing radius (Frank 1977; Bogner et al. 2000; Eastin et al. 2005). With higher CAPE and a lower altitude of strong convergence, the outer cell updraft is likely more buoyant than the inner cell, accelerating the air upward at greater speeds and to higher altitudes. On the other hand, the inner cell is in a region of less CAPE and has strong convergence largely above the mixed layer, all of which points to decreased buoyancy and weaker updrafts. Barnes (2008) found instances where equivalent potential temperature temporarily increased with height above the inflow layer, which can contribute to the buoyant uplift within inner convective cells. Some amount of CAPE is necessary to trigger the inner convective cell; however, the slanted nature of the divergence/convergence couplet and the updraft suggests that the circulation can be partially (if not mostly) attributed to slantwise neutral forced ascent in a manner similar to the eyewall (Emanuel 1986; Houze 1993, ch. 10; Rogers et al. 2012), but on a much smaller scale. Entrainment may also play a significant role in decreasing the buoyancy of the rising air (Zipser 2003; Eastin et al. 2005), particularly in the inner cells where the wind shear is higher; but buoyancy reduction via entrainment becomes less pertinent in an environment of increasing slantwise neutral forced ascent.

b. Radial momentum budget analysis

Figure 7 shows the average vertical profile of radial and tangential velocity in the inner and outer convective regions. As seen in the cross-section composite, the low-level radial inflow in the inner region is stronger and declines sharply with height, while the inflow layer in the outer region is deeper and has a more gradual decline. Also, the outer region tangential wind has

a more elevated maximum, consistent with the midlevel jet occurrences. The differences between the inner and outer regions can be partially explained by results from the theoretical and modeling studies of Kepert (2001) and Kepert and Wang (2001). In a steady-state tropical cyclone, the maximum tangential wind is a low-level supergradient flow maintained by a balance between vertical diffusion and vertical advection, and it is associated with strong inflow beneath, and weak outflow above. According to these ideas, as wind velocities increase inward, the inflow depth and the altitude of the maximum tangential wind must decrease. In our analysis, the depth of the inflow layer and the altitude of the maximum tangential wind indeed decrease radially inward. In the following discussions, we define the top of the tropical cyclone boundary layer as the altitude of the maximum axisymmetric tangential wind. In their studies, Kepert (2001) and Kepert and Wang (2001) purposely neglected the impact of convective-scale processes. We address convective-scale processes here by examining the instantaneous momentum tendencies of the kinematic field.

The radial momentum equation in cylindrical coordinates (r,θ,z) is given by

$$\frac{\partial u}{\partial t} = -u\frac{\partial u}{dr} - \frac{v}{r}\frac{\partial u}{\partial \theta} - w\frac{\partial u}{\partial z} + \frac{v^2}{r} + fv - \frac{1}{\rho}\frac{\partial p}{\partial r} + F_r \,, \tag{1}$$

where u, v, and w are the radial, tangential, and vertical velocities, p is pressure, ρ is density, and f is the Coriolis parameter. The right-hand-side terms represent radial advection, azimuthal advection, vertical advection, centrifugal acceleration, Coriolis acceleration, pressure gradient acceleration, and dissipation. Calculations of azimuthal advection yield non-negligible values, but this term was prone to erratic behavior, which was likely due to large sampling errors with the azimuthal derivative; small errors in tangential wind produce large magnitude errors in $\partial u/\partial t$. Furthermore, without observations of the total storm, the azimuthal advection term is heavily influenced by changes associated with low-wavenumber features, making calculations of this

term less useful in investigating convective-scale features. For these reasons, we decided not to consider azimuthal advection in our analysis. Frictional dissipation is certainly important to the momentum budget; however, this term cannot be calculated with the current dataset. We consider the effects of friction throughout the following discussions.

I. Assumption of Gradient Balance

Above the tropical cyclone boundary layer, the radial flow is approximately in gradient balance, which designates the sum of the pressure gradient, centrifugal, and Coriolis terms to be zero (the total derivative of radial velocity is also zero). When a heat source is placed in an idealized axisymmetric vortex in gradient balance, the vortex responds by developing an overturning circulation where radial inflow near the surface turns upward through the heat source and travels radially outward above (Shapiro and Willoughby 1982). Moon and Nolan (2010) demonstrated with idealized simulations that a similar overturning circulation occurs on a local scale for an asymmetric heat source located within a tropical cyclone vortex (e.g. rainband convective cells). According to their calculations, the secondary circulations associated with the current observed rainband cells (Figs. 3, 4) exhibit the circulation pattern that is expected for a heat source within a vortex in gradient balance. It follows that under the assumption of gradient balance, the evolution of the radial wind (described by Eq. 1) within the rainbands above the boundary layer is determined primarily by the advection terms.

Figure 8 shows the average vertical profiles of the radial and vertical advection terms contributing to $\partial u/\partial t$, and Figure 9 shows their total. The total tendencies reach minima, indicating a maximum increase in radial inflow, at 3 km and 6 km altitudes for the inner and outer regions respectively. The largest contribution to these minima comes from the vertical advection term, followed by the radial advection term that peaks at a slightly higher altitude. The

radial outflow layers in Figs. 3a and 4a occur mostly in altitudes above their corresponding minimum in vertical advection. This association in the context of an overturning circulation indicates that vertical advection determines the minimum altitude of the radial outflow. Moreover, the larger buoyant acceleration in the outer cell yields a deeper and stronger updraft that advects the radial outflow branch of the overturning circulation to a higher level than that seen in the inner cell.

A lower-level outflow layer owing to shallower vertical advection in inner cells culminates in a sharp increase in radial wind with altitude (i.e. large $\partial u/\partial z$), like that seen in Fig. 7a; nevertheless, other factors also contribute to the different radial wind profiles for the inner and outer regions. As described by the Sawyer-Eliassen equations, a heat source under large inertial stability induces a vertically-elongated overturning circulation with weak radial winds (Eliassen 1951; Schubert and Hack 1982). Inner convective cells under larger inertial stability would be expected to exhibit this weaker circulation, and thus weaker $\partial u/\partial z$, in the absence of a frictional inflow layer; however, as part of the larger vortex circulation, frictional inflow is stronger in the inner region which enhances $\partial u/\partial z$ for cells at smaller radii. The depth of the inflow layer, which is shallower at smaller radii, also contributes to a larger $\partial u/\partial z$. The differing values of $\partial u/\partial z$ will become important in later discussions.

II. LOCAL IMBALANCE OF RADIAL FORCES

The circulations associated with rainband cells are perturbations to the axisymmetric storm structure that can lead to a departure from gradient balance. Such an imbalance can occur when strong updrafts of a convective cell advect tangential winds upward from the boundary layer into levels where the background pressure gradient weakens with height. Thus, the kinematics associated with rainband cells may locally disturb gradient balance by increasing the

tangential velocity more rapidly than the pressure field can adjust. We define the gradient balance residual (GBR) as

$$\mathrm{GBR} = \frac{v^2}{r} + fv - \frac{1}{\rho}\frac{\partial p}{\partial r}\ , \tag{2}$$

where positive GBR values denote supergradient flow and outward acceleration and negative values denote subgradient flow and inward acceleration.

We calculate the GBR field for the inner convective cells using a combination of dropsonde and Doppler radar measurements. Dropsonde coverage was not sufficient for a similar analysis of the outer convective cells. Pressure readings from the dropsondes were first fit to a second-degree polynomial under the assumption that an individual pressure measurement represented an axisymmetric value. The GBR field was calculated using the analytical derivative of this polynomial, densities from a standard tropical Atlantic atmosphere (Jordan 1958), and velocities from the Doppler radar data. Figure 10 shows the GBR field for the composite inner convective cell. GBR values are positive everywhere and highest within the convective cell where tangential winds are elevated. These increased GBR values correspond to increased outward acceleration and supergradient flow as a result of the local tangential wind perturbations within the convective cell.

If a perturbation, δv, is added to the tangential velocity in Eq. 2 and the pressure gradient term remains unchanged, then the GBR value would increase by

$$\frac{2v\delta v}{r} + \frac{(\delta v)^2}{r} + f\delta v,$$

which is the rate of increased outward acceleration. Given the overlap of tangential jet magnitudes for the inner and outer region cells (Fig. 5), it appears feasible that cells in both regions can produce low-level δv perturbations of similar magnitudes. In the case where δv is

equal for both regions, the supergradient outward acceleration is always greater for the inner region because of the larger *v* and smaller *r*. As inner regions have smaller vertical velocities due to less buoyant acceleration, a rising air parcel that swiftly accelerates outward would result in a radial outflow layer at a lower altitude. This effect would further enhance $\partial u/\partial z$ for inner convective cells. Conversely, outer cells with stronger buoyant acceleration and a weaker supergradient response would lead to a higher outflow layer.

A local imbalance of radial forces can also arise from pressure perturbations induced by the rainband convective cells. Pressure perturbations have been observed in the low and midlevels of rainband cells and were attributed to either hydrostatic or dynamic forcing (Powell 1990a; Barnes et al. 1991). Hydrostatic pressure perturbations result from the buoyancy of an air parcel, which relates to the CAPE of the environment. A buoyant updraft in a rainband cell would produce an anomalous negative radial pressure gradient along its inner side. Dynamic pressure perturbations are related to the interaction of a vertical velocity perturbation with the vertical wind shear by

$$p' \propto \frac{d\mathbf{V}}{dz} \cdot \nabla_H w', \tag{3}$$

where **V** is the horizontal wind vector and ∇_H is the horizontal gradient operator (Rotunno and Klemp 1982; Houze 1993, ch. 8). Through this relationship, a rainband updraft in the presence of positive vertical shear of the radial wind ($\partial u/\partial z > 0$) would produce an anomalous negative radial pressure gradient through the updraft. In the case of either hydrostatic of dynamic pressure perturbations, the anomalous pressure gradient would increase the GBR value on the inner side of the convective cell. Both tangential velocity perturbations and expected pressure perturbations act to increase outward acceleration associated with the supergradient flow along the inner side of a rainband convective cell.

c. Tangential momentum budget analysis

The tangential momentum equation is given by

$$\frac{\partial v}{\partial t} = -u\frac{\partial v}{dr} - \frac{v}{r}\frac{\partial v}{\partial \theta} - w\frac{\partial v}{\partial z} - \frac{uv}{r} - fu - \frac{1}{\rho}\frac{\partial p}{\partial \theta} + F_\theta \,, \tag{4}$$

where the right-hand-side terms represent radial advection, azimuthal advection, vertical advection, angular momentum conservation, Coriolis acceleration, pressure gradient acceleration, and dissipation. High-wavenumber pressure perturbations introduce azimuthal pressure gradients that can affect the convective-scale rainband structure. These effects may be significant to the tangential momentum tendency, but detailed pressure measurements were not available. We expect that hydrostatic pressure perturbations would induce tangential accelerations similar to vertical advection since they are both related to the buoyancy of air parcels. Additionally, dynamic pressure perturbations introduced by updrafts [following Eq. (3)] would yield positive tangential acceleration only in the boundary layer where $\partial v/\partial z < 0$. We ignore the azimuthal advection term and frictional dissipation terms for the same reasons discussed in the radial momentum budget analysis.

Figure 11 presents the average vertical profiles of the tangential momentum budget terms for the inner and outer convective regions. The angular momentum conservation (uv/r) and Coriolis terms follow the opposite sign and relative magnitude of the radial velocity throughout the vertical profile. Eq. (4) indicates this relationship since u is a coefficient in both terms, and v/r and f are always positive. In the inner region, these two terms are positive below 1.5 km altitude and decrease sharply with height in agreement with the large $\partial u/\partial z$. In the outer region, the uv/r and Coriolis terms have smaller values in the lowest level that then decrease more gradually with height (following a smaller $\partial u/\partial z$) while remaining positive through a depth of 4 km. The radial advection term has a sign that largely mirrors the uv/r and Coriolis terms since

$\partial v/\partial r$ is mostly negative, but its range of magnitudes changes little between the inner and outer regions. The vertical advection term in both regions is mostly positive below 9 km containing multiple peaks in magnitude. The largest peaks in both regions have similar values; however, the peak for the outer cell occurs 3 km higher than the peak for the inner cell, which is consistent with the deeper and stronger updrafts in the outer cells.

The total tendencies are displayed in Fig. 12. For the inner region, the shape of the total profile is mostly aligned with the uv/r term, which decreases rapidly with height. The maximum strengthening of momentum occurs in the lowest levels where uv/r and vertical advection have the same sign and similar magnitudes. Above 2 km, the uv/r term turns negative and remains much greater in magnitude than the vertical advection term, which yields a convincing reduction in momentum production by the convective-scale motions at these altitudes. In the outer region, the difference between uv/r and vertical advection is smaller and thus the two terms jointly determine the general shape of the total profile. Momentum is increasing from the low levels through 7 km altitude, with local maxima of similar rates occurring near 2, 3, and 6 km altitudes. Compared to the tangential wind profiles (Fig. 7b), the inner region tendency is strengthening and sharpening the low-level jet, while the outer region tendency indicates both strengthening of its low-level jet and building of a midlevel jet (or jets).

These radial and tangential momentum analyses demonstrate that the vortex-scale dynamics are responsible for the differing convective-scale radial and tangential wind signatures in the inner and outer regions. Convective cells at smaller radii experience stronger frictional inflow, and weaker, shallower updrafts. The resulting overturning circulation is shallower and $\partial u/\partial z$ is larger, causing tangential acceleration due to angular momentum conservation to outweigh the effect of vertical advection and constrain the tangential wind perturbation

maximum to a low altitude. In the outer region, deeper, stronger updrafts in an environment of higher CAPE and weaker radial inflow allow for tangential acceleration due to angular momentum conservation and vertical advection in overturning convective cells to substantially increase the tangential winds at multiple altitudes, creating the possibility of a jet occurring in the low or midlevels.

5. Azimuthal evolution of convection

The discussion in Section 4 makes clear that the vortex-scale circulation affects the shape of the radial wind profile in convective-scale features. However, the extent of the contribution from the convective-scale radial wind to the vortex-scale circulation remains unclear. To evaluate this contribution, the radial wind from the entire area was azimuthally averaged over sections A and B and the result is presented in Fig. 13. The inner and outer convective cells, indicated by the reflectivity towers, coincide with decay of the deep inflow layer and enhancement of the outflow at different altitudes, as shown in the composites (Figs. 3a, 4a). The changes in the radial wind at locations of active convective cells suggest that the cells are actively shaping the larger-scale radial wind profile. Specifically, this large scale pattern may result from the aggregate of convective-scale heat sources that drive deep radial inflow and enhanced radial outflow in the same manner as the convective rainband simulated by Moon and Nolan (2010).

Since the vertical shear of radial wind is critical in determining the altitudes of tangential jets, we expect that changes in the radial wind and tangential wind profiles will be closely linked in their azimuthal evolution. Figures 14 and 15 present the average profiles of the radial and tangential winds in the inner and outer regions for sections A-D. In the upwind sections A and B,

the radial and tangential wind profiles are similar to their corresponding profiles in just the convective areas (Fig. 7). In section A, the radial wind of the inner region increases more rapidly with height than that of the outer region through a depth of 5 km altitude. For section B, this difference in the rate of change remains apparent but is less pronounced. The tangential wind maxima in sections A and B lie at a higher altitude for the outer region. The differences seen in these profiles are consistent with the dynamical explanations presented in Section 4. This analysis further indicates that convective cell kinematics impacts the circulation over a region larger than that inhabited by the cells.

The downwind sections C and D exhibit a marked change in the radial wind; the inflow below 2 km decreases rapidly with height in both regions, and the inner region radial wind remains more negative than the outer region through most of the troposphere. As the convection spirals inward to sections C and D, the tangential winds seen in Fig. 15 become stronger with maxima occurring at lower altitudes for both regions. In contrast to the disparity of the inner and outer upwind profiles, the increasing similarity in the shapes of the inner and outer downwind profiles reflects the decreased occurrences of robust convection in the downwind zones of rainbands. Without the different depths of the overturning circulations associated with active convection, the radial winds in both regions have similar changes with height. Furthermore, in the absence of frequent buoyant updrafts, the maximum tangential wind can remain at low altitudes, aligning with the steady-state circulation examined in Kepert (2001) and Kepert and Wang (2001). In section D, a deep layer of decreased radial wind occurs in the midlevels for both inner and outer regions. This feature, which persists on the western side of the storm, will be explored in a future paper.

6. Implications for secondary eyewall formation

The secondary eyewall is a ring of heavy precipitation collocated with a well-defined wind maximum that sometimes forms outside a pre-existing primary eyewall. Although past studies have proposed several factors to be essential for secondary eyewall formation (e.g. Nong and Emanuel 2003; Montgomery and Kallenbach 1997; Kuo et al. 2004; Terwey and Montgomery 2008; Judt and Chen 2010; Qiu et al. 2010; Huang et al. 2012), the initial formation mechanism remains unclear. Nevertheless, modeling studies and observations agree that the process begins when convective elements persistently populate a certain broad region outside of the primary eyewall. Being associated with rainbands, this convection spirals inward and axisymmetrizes. The dynamical explanation for the observations in this study is applicable to all tropical cyclones, including those that do not form a secondary eyewall. Still, these results may provide insight to the mechanisms that lead to secondary eyewall formation since Rita developed a mature secondary eyewall just 12 h after the time of the observations.

Didlake and Houze (2011) examined the structure of Rita's secondary eyewall and found enhanced radial outflow just above the boundary inflow layer, which modified the deeper overturning circulation in a pattern similar to observed primary eyewalls (e.g. Bell and Montgomery 2008). This enhanced low-level outflow was associated with a low-level tangential wind maximum, which was confirmed to be strongly supergradient. Huang et al. (2012) examined the axisymmetric processes associated with the secondary eyewall development in Typhoon Sinlaku (2008). After an expansion of the tangential wind field of the vortex, they found that the tangential winds within and just above the boundary inflow layer became increasingly more supergradient, which resulted in decelerated radial inflow, increased convergence, and enhanced convection in a concentrated region outside of the eyewall. The

shallow overturning circulation and low-level tangential jet from Didlake and Houze (2011) strongly resemble the structures presently observed in the inner convective cells, suggesting a dynamical similarity between the two; moreover, the processes described by Huang et al. (2012) comprise a dynamical explanation that possibly connects the evolution of these features. Bell et al.'s (2012) axisymmetric analysis of Rita's secondary eyewall development supports the dynamical framework of Huang et al. (2012). Other studies (i.e. Judt and Chen 2010; Qiu et al. 2010) argue that a secondary eyewall forms when a sufficient number of convective cells, represented as potential vorticity anomalies, inhabit a narrow annular ring. Based on results from the above-mentioned studies and the current study, we place a larger emphasis on the convective cells' kinematic structure rather than their amount or coverage for triggering secondary eyewall formation, as cells with a certain *structure* will favor the amplification of convection and eventual axisymmetrization.

The presence of convectively enhanced supergradient flow at low levels is an indicator of the convective cell's ability to continue strengthening and/or produce new convection. Supergradient flow can be enhanced by either producing a tangential jet or decreasing the radial pressure gradient (as explained in Section 4b). Convective cells containing a tangential jet or decreased radial pressure gradient in the boundary layer will experience outward acceleration that is larger than the boundary layer supergradient acceleration of a steady-state vortex (Kepert 2001; Kepert and Wang 2001). As a result, the outwardly accelerating flow will locally enhance low-level convergence, upward motion, and convection. A low-level tangential jet will also increase surface fluxes of moisture and possibly enhance the wind-induced surface heat exchange (WISHE; Yano and Emanuel 1991) feedback; however, recent studies suggest that regions of low-level convergence and their associated convection play a more dominant role than

the WISHE feedback in amplifying the storm (Nguyen et al. 2008; Montgomery et al. 2009). Convective cells containing supergradient flow at higher altitudes will also induce outward acceleration; however, any associated convergence at these levels may not enhance upward motion to feed the convection.

It follows that convective cells that spiral inward can enter a critical zone in which secondary eyewall formation becomes favorable due to their inherent convective-scale dynamics. Within this critical zone, the vertical gradient of radial wind throughout the low to mid-troposphere becomes strong enough such that convective cells consistently produce supergradient flow within the boundary layer, which can subsequently intensify or favor the development of convection. If a convective cell contains a weakly buoyant updraft, then a large $\partial u/\partial z$ will confine the convectively generated tangential jet to a low altitude by ensuring that the vertical profile of tangential acceleration is dominated by the angular momentum conservation term and not vertical advection. If a convective cell contains a strongly buoyant updraft, then a large $\partial u/\partial z$ will enhance dynamic pressure perturbations associated with the updraft such that the radial pressure gradient is locally decreased. Both processes depend on the strength of $\partial u/\partial z$ to facilitate enhancement of the low-level supergradient flow. Furthermore, both processes can occur in the life span of a single convective cell, promoting the maintenance of this cell and creation of new convection. This hypothesis is similar to the beta-skirt mechanism of Terwey and Montgomery (2008) in that it describes a favored region for secondary eyewall formation where the vortex circulation is sufficiently robust and CAPE is present for the production of convective cells. But, instead of highlighting the radial gradient of vorticity, we emphasize the vertical gradient of radial wind as a key property of the vortex circulation for secondary eyewall formation.

The factors determining the inner boundary of the critical zone remain unclear from the current dataset; however, a secondary eyewall must be sufficiently far from the primary eyewall for both circulations to exist simultaneously. We speculate that a natural boundary forms once the tangential jet and overturning circulation axisymmetrize at a given radius, as this incipient secondary eyewall circulation seems to require subsidence and formation of an eye-like moat radially inward (Houze et al. 2007). This critical zone hypothesis may explain why a secondary eyewall forms mostly in major tropical cyclones, as the critical zone can only exist in inner cores of sufficiently strong boundary layer inflow. Furthermore, this wind speed dependence may also explain why secondary eyewall formation appears to be preceded by a significant expansion of the vortex wind field (Qiu et al. 2010; Huang et al. 2012; Bell et al. 2012), which could represent an increase in the extent of the critical zone.

The outflow branch of a convective cell's circulation may also contribute to enhancing convection. Figure 16 shows the reflectivity field observed during 2010-2032 UTC. A nearly continuous band of precipitation containing robust convection spiraled around the storm between 50-100 km distance from the vortex center. Bell et al. (2012) point to this rainband as a precursor to the secondary eyewall formed on the next day. The deep convective cells occurring on its upwind end are tightly packed and exhibit a double-banded structure. Figure 17 presents an averaged radial cross section of these cells. Cell A contains enhanced radial outflow on its outer side at 3 km altitude, which appears to be interacting with the circulation of Cell B. The local minimum of radial divergence (Fig. 17c) near 88 km radius and 2.5 km altitude indicates convergence associated with radial outflow of Cell A. The corresponding convergence signal in the total divergence field (Fig. 17d) reflects the significance of the radial divergence to the local vertical velocity. In the secondary eyewall, shallow radial outflow extending to 3 km altitude

converged with deep inflow approaching from radially outside, which directly enhanced upward motion of the overturning circulation (Didlake and Houze 2011). In this rainband, a divergence/convergence couplet exists at 86-95 km radius beneath the radial outflow convergence. This pattern is consistent with a downdraft initiated by the radial outflow of Cell A, which diverges at the surface and induces convergence radially outward. Consequently, upward motion is initiated to create Cell B of this rainband. The regularity of this exact pattern within the rainband is not known; however, its existence and similarity to the secondary eyewall indicates that shallow overturning circulations can indeed interact with outside radial inflow to produce net convergence. Furthermore, this convergence can be translated into upward motion and enhanced convection. The dynamics of these rainband cells are similar to the axisymmetric dynamics of a developing and mature secondary eyewall (Huang et al. 2012; Didlake and Houze 2011). This similarity provides further support for the idea that these inner rainband cells are the beginning elements of secondary eyewall development.

7. Conclusions

The NCAR ELDORA radar system collected high-resolution reflectivity and velocity observations of the inner-core rainbands in Hurricane Rita (2005). We have analyzed the radial and azimuthal variability in the structures of this inner-core convection. Azimuthal variations generally reflect the changing thermodynamic structure and differential advection of hydrometeors along rainbands spiraling around the storm. The upwind portion of the rainband tends to comprise discrete or connected convective cells supported by sufficient conditional instability. As the available instability depletes traveling along the rainband, convective cells become fewer and weaker. The downwind portion of the rainband contains mostly stratiform

precipitation as slowly falling ice particles produced by the upwind convective cells are advected downwind. The organization of the rainbands follows results from past studies that link the azimuthal orientation to the environmental vertical wind shear. At larger (smaller) radii, convective cells are most prevalent in the downshear right (left) quadrant, and stratiform precipitation proliferates downwind of the convective cells.

The active cells in the upwind region have significant radial variability that is summarized in the conceptual model shown in Fig. 18. This cross section schematic represents two convective cells and their associated convective-scale structures at different radii within the inner core. Low-level radial inflow as part of the larger vortex-scale circulation approaches Cell 1 and Cell 2, and then turns upward through each reflectivity tower. A momentum budget analysis indicates that angular momentum conservation (*uv/r* term) and vertical advection strengthen the low-level tangential winds in both cells, as indicated by the plus signs. Local tangential wind maxima, denoted as V_1 and V_2, are thus produced. Consistent with the predicted steady-state vortex-scale circulation (Kepert 2001; Kepert and Wang 2001), the boundary layer inflow depth and the base of the tangential wind jets decrease as the radial inflow strengthens at smaller radii. The updraft of Cell 1 is weaker and more tilted, while the updraft of Cell 2 is more buoyant and upright, resulting in radial outflow at a higher altitude. Tangential acceleration owing to angular momentum conservation outweighs vertical advection in Cell 1 because of the stronger vertical gradient of radial wind at the more inward radius. As a result, the shallow radial outflow weakens the tangential winds (the minus signs in Figure 18 indicate the weakening), and V_1 is confined to the low levels. In Cell 2, deeper radial inflow and stronger vertical advection strengthen the tangential wind at higher levels, allowing for V_2 to range from the low to midlevels, or occupy multiple levels as illustrated in the schematic. These tangential jets, along

with pressure perturbations generated by the updraft, create increased supergradient flow within the convective cells. When such increased supergradient flow occurs in the low levels, as in tangential jet V_1, the boundary layer inflow decelerates and enhances low-level convergence on its radially outward side; consequently, the supergradient flow enhances upward motion and inner-core convection.

This analysis of convective cells in the inner-core region of tropical cyclones brings new insight to the dynamics of secondary eyewall formation. Previous observations show that secondary eyewalls take on their continuous ring shape with the axisymmetrization of inner-core convective elements. We hypothesize that a critical zone for this formation process exists where the vertical gradient of radial wind in the low to mid-troposphere becomes strong enough such that convectively enhanced supergradient flow consistently remains low in altitude to enhance convergence of the boundary layer inflow. This idea is consistent with the secondary eyewall's radar echo having a highly cellular structure in contrast to the smoother appearance of the primary eyewall. Once an incipient secondary eyewall forms at a certain radius, subsidence and moat formation occurs along its inner edge as part of the overall secondary eyewall dynamics and thus separates the secondary eyewall from the primary eyewall.

Several aspects of this study should be explored in future research. A similar analysis of inner-core convection from other observed and simulated storms is needed to determine the generality of the convective-scale variability within rainband structures. Using full-physics models running with sufficiently high resolution to produce secondary eyewalls, the critical zone hypothesis needs to be examined further, so it can be verified or rejected. The pressure perturbation field, thermodynamic structure, and boundary layer processes also need further investigation, as all aspects were limitations in the current study.

Acknowledgments

We are thankful for the help and comments of Stacy Brodzik, Greg Hakim, Deanna Hence, Wen-Chau Lee, Bradley Smull, Angeline Pendergrass, John M. Wallace, and Michael Bell. Dr. Bell provided the vortex centers and valuable guidance with radar data processing and interpretation. Comments from Gary Barnes, Ed Zipser, and an anonymous reviewer brought significant improvements to the manuscript. Beth Tully assisted with graphics and editing. This research was supported by the National Science Foundation under Grants ATM-0432623 and ATM-0743180, and the Department of Defense through the National Defense Science and Engineering Graduate Fellowship Program.

References

Atlas, D., K. R. Hardy, R. Wexler, and R. J. Boucher, 1963: On the origin of hurricane spiral bands. *Geofis. Int.* **3,** 123-132.

Barnes, G. M., 2008: Atypical thermodynamic profiles in hurricane. *Mon. Wea. Rev.,* **136,** 631-643.

Barnes, G. M., and G. J. Stossmeister, 1986: The structure and decay of a rainband in Hurricane Irene (1981). *Mon. Wea. Rev.*, **114,** 2590-2601.

Barnes, G. M., and M. D. Powell, 1995: Evolution of the inflow boundary layer of Hurricane Gilbert (1988). *Mon. Wea. Rev.*, **123**, 2348-2368.

Barnes, G. M., E. J. Zipser, D. Jorgensen, and F. Marks Jr., 1983: Mesoscale and convective structure of a hurricane rainband. *J. Atmos. Sci.*, **40,** 2125-2137.

Barnes, G. M., J. F. Gamache, M. A. LeMone, and G. J. Stossmeister, 1991: A convective cell in a hurricane rainband. *Mon. Wea. Rev.,* **119,** 776-794.

Bell, M. M., and M. T. Montgomery, 2008: Observed structure, evolution, and potential intensity of category 5 Hurricane Isabel (2003) from 12 to 14 September. *Mon. Wea. Rev.,* **136,** 2023-2046.

Bell, M. M., M. T. Montgomery, and W.-C. Lee, 2012: An axisymmetric view of concentric eyewall evolution in Hurricane Rita (2005). *J. Atmos. Sci.,* in press.

Beven II, J. L., and Coauthors, 2008: Atlantic hurricane season of 2005. *Mon. Wea. Rev.*, **136**, 1109-1173.

Bogner, P. B., G. M. Barnes, and J. L. Franklin, 2000: Conditional instability and shear for six hurricanes over the Atlantic Ocean. *Wea. Forecasting*, **15**, 192-207.

Bosart, B. L., W.-C. Lee, and R. M. Wakimoto, 2002: Procedures to improve the accuracy of airborne Doppler radar data. *J. Atmos. Oceanic Technol.,* **19,** 322-339.

Burpee, R. W., and M. L. Black, 1989: Temporal and spatial variations of rainfall near the centers of two tropical cyclones. *Mon. Wea. Rev.*, **117**, 2204-2218.

Chen, S. S., J. A. Knaff, and F. D. Marks Jr., 2006: Effects of vertical wind shear and storm motion on tropical cyclone rainfall asymmetries deduced from TRMM. *Mon. Wea. Rev.,* **134,** 3190-3208.

Churchill, D. D., and R. A. Houze Jr., 1984: Development and structure of winter monsoon cloud clusters on 10 December 1978. *J. Atmos. Sci.,* **41,** 933-960.

Corbet, J., C. Mueller, C. Burghart, K. Gould, and G. Granger, 1994: Zeb: Software for integration, display and management of diverse environmental datasets. *Bull. Amer. Meteor. Soc.,* **75,** 783-792.

Corbosiero, K. L., and J. Molinari, 2002: The effects of vertical wind shear on the distribution of convection in tropical cyclones. *Mon. Wea. Rev.,* **130,** 2110-2123.

Corbosiero, K. L., and J. Molinari, 2003: The relationship between storm motion, vertical wind shear, and convective asymmetries in tropical cyclones. *J. Atmos. Sci.,* **60,** 366-460.

Corbosiero, K. L., J. Molinari, A. R. Aiyyer, and M. L. Black, 2006: The structure and evolution of Hurricane Elena (1985). Part II: Convective asymmetries and evidence for vortex Rossby waves. *Mon. Wea. Rev.,* **134,** 3073-3091.

Didlake, A. C., Jr., and R. A. Houze Jr., 2009: Convective-scale downdrafts in the principal rainband of Hurricane Katrina (2005). *Mon. Wea. Rev.,* **137,** 3269-3293.

Didlake, A. C., Jr., and R. A. Houze Jr., 2011: Kinematics of the secondary eyewall observed in Hurricane Rita (2005). *J. Atmos. Sci.,* **68,** 1620-1636.

Eastin, M. D., W. M. Gray, and P. G. Black, 2005: Buoyancy of convective vertical motions in the inner core of intense hurricanes. Part I: General statistics. *Mon. Wea. Rev.,* **133**, 188-208.

Eliassen, A., 1951: Slow thermally or frictionally controlled meridional circulation in a circular vortex. *Astrophys. Norv.,* **5,** 19-60.

Emanuel, K. A., 1986: An air-sea interaction theory for tropical cyclones. Part I: Steady-state maintenance. *J. Atmos. Sci.* **43,** 585-604.

Frank, W. M., 1977: The Structure and energetics of the tropical cyclone I. Storm Structure. *Mon. Wea. Rev.,* **105**, 1119-1135.

Frank, W. M., 1984: A composite analysis of the core of a mature hurricane. *Mon. Wea. Rev.,* **112**, 2401-2420.

Hence, D. A., and R. A. Houze Jr., 2008: Kinematic structure of convective-scale elements in the rainbands of Hurricanes Katrina and Rita (2005). *J. Geophys. Res.,* **113,** D15108, doi:10.1029/2007JD009429.

Hence, D. A., and R. A. Houze Jr., 2011: Vertical structure of hurricane eyewalls as seen by the TRMM Precipitation Radar. *J. Atmos. Sci.,* **68**, 1637-1652.

Hence, D. A., and R. A. Houze Jr., 2012: Vertical structure of tropical cyclone rainbands. *J. Atmos. Sci.,* in press.

Hildebrand, P. H., and Coauthors, 1996: The ELDORA/ASTRAIA airborne Doppler weather radar: High-resolution observations from TOGA COARE. *Bull. Amer. Meteor. Soc.,* **77,** 213-232.

Houze, R. A., Jr., 1993: *Cloud Dynamics.* Academic Press, 573 pp.

Houze, R. A., Jr., 1997: Stratiform precipitation in regions of convection: A meteorological paradox? *Bull. Amer. Meteor. Soc.,* **78,** 2179-2196.

Houze, R. A., Jr., 2010: Clouds in tropical cyclones. *Mon. Wea. Rev.*, **138,** 293-344.

Houze, R. A., Jr., and Coauthors, 2006: The Hurricane Rainband and Intensity Change Experiment: Observations and modeling of Hurricanes Katrina, Ophelia, and Rita. *Bull. Amer. Meteor. Soc.,* **87,** 1503-1521.

Houze, R. A., Jr., S. S. Chen, B. F. Smull, W.-C. Lee, and M. M. Bell, 2007: Hurricane intensity and eyewall replacement. *Science,* **315,** 1235-1239.

Huang, Y.-H., M. T. Montgomery, and C.-C. Wu, 2012: Concentric eyewall formation in Typhoon Sinlaku (2008). Part II: Axisymmetric dynamical processes. *J. Atmos. Sci.,* **69,** 662-674.

James, C. N., S. R. Brodzik, H. Edmon, R. A. Houze Jr., and S. E. Yuter, 2000: Radar data processing and visualization over complex terrain. *Wea. Forecasting,* **15**, 327-338.

Jordan, C. L., 1958: Mean soundings for the West Indies area. *J. Atmos. Sci.,* **15,** 91-97.

Judt, F., and S. S. Chen, 2010: Convectively generated potential vorticity in rainbands and formation of the secondary eyewall in Hurricane Rita of 2005. *J. Atmos. Sci.,* **67**, 3581-3599.

Kepert, J., 2001: The dynamics of boundary layer jets within the tropical cyclone core. Part I: Linear theory. *J. Atmos. Sci.*, **58**, 2469-2484.

Kepert, J. D., 2006a: Observed boundary layer wind structure and balance in the hurricane core. Part I: Hurricane Georges. *J. Atmos. Sci.*, **63**, 2169-2193.

Kepert, J. D., 2006b: Observed boundary layer wind structure and balance in the hurricane core. Part II: Hurricane Mitch. *J. Atmos. Sci.*, **63**, 2194-2211.

Kepert, J., and Y. Wang, 2001: The dynamics of boundary layer jets within the tropical cyclone core. Part II: Nonlinear enhancement. *J. Atmos. Sci.,* **58**, 2485-2501.

Kuo, H.-C., L.-Y. Lin, C.-P. Chang, and R. T. Williams, 2004: The formation of concentric vorticity structures in typhoons. *J. Atmos. Sci.,* **61,** 2722-2734.

Lonfat, M., F. D. Marks Jr., and S. S. Chen, 2004: Precipitation distribution in tropical cyclones using the Tropical Rainfall Measuring Mission (TRMM) microwave imager: A global perspective. *Mon. Wea. Rev.*, **132**, 1645-1660.

Marks, F. D., Jr., and L. K. Shay, 1998: Landfalling tropical cyclones: Forecast problems and associated research opportunities. *Bull. Amer. Meteor. Soc.,* **79,** 305-323.

Marks, F. D., Jr., R. A. Houze Jr., and J. F. Gamache, 1992: Dual-aircraft investigation of the inner core of Hurricane Norbert. Part I: Kinematic structure. *J. Atmos. Sci.*, **49**, 919-942.

Mohr, C. G., L. J. Miller, R. L. Vaughan, and H. W. Frank, 1986: The merger of mesoscale datasets into a common Cartesian format for efficient and systematic analyses. *J. Atmos. Oceanic Technol.*, **3**, 143-161.

Montgomery, M. T., and R. J. Kallenbach, 1997: A theory for vortex Rossby-waves and its application to spiral bands and intensity changes in hurricanes. *Quart. J. Roy. Meteor. Soc.,* **123,** 435-465.

Montgomery, M. T., S. V. Nguyen, R. K. Smith, and J. Persing, 2009: Do tropical cyclones intensify by WISHE? *Quart. J. Roy. Meteor. Soc.*, **135,** 1697-1714.

Moon, Y., and D. S. Nolan, 2010: The dynamic response of the hurricane wind field to spiral rainband heating. *J. Atmos. Sci.,* **67,** 1779-1805.

Nguyen, S. V., R. K. Smith, and M. T. Montgomery, 2008: Tropical-cyclone intensification and predictability in three dimensions. *Quart. J. Roy. Meteor. Soc.,* **134,** 563-582.

Nong, S., and K. Emanuel, 2003: A numerical study of the genesis of concentric eyewalls in hurricanes. *Quart. J. Roy. Meteor. Soc.,* **129,** 3323-3338.

Oye, D., and M. Case, 1994: REORDER: A program for gridding radar data. [Available online at http://www.eol.ucar.edu/rsf/UserGuides/ELDORA/DataAnalysis/reorder/unixreorder.ps]

Oye, R., C. Mueller, and S. Smith, 1995: Software for radar translation, visualization, editing, and interpolation. Preprints, *27th Conf. on Radar Meteorology,* Vail, CO, Amer. Meteor. Soc., 359-363.

Powell, M. D., 1990a: Boundary layer structure and dynamics in outer hurricane rainbands. Part I: Mesoscale rainfall and kinematic structure. *Mon. Wea. Rev.,* **118,** 891-917.

Powell, M. D., 1990b: Boundary layer structure and dynamics in outer hurricane rainbands. Part II: Downdraft modification and mixed layer recovery. *Mon. Wea. Rev.,* **118,** 918-938.

Qiu, X., Z.-M. Tan, and Q. Xiao, 2010: The roles of vortex Rossby waves in hurricane secondary eyewall formation. *Mon. Wea. Rev.,* **138,** 2092-2109.

Reasor, P. D., M. D. Eastin, and J. F. Gamache, 2009: Rapidly intensifying Hurricane Guillermo (1997). Part I: Low-wavenumber structure and evolution. *Mon. Wea. Rev.,* **137,** 603-631.

Rogers, R., S. Lorsolo, P. Reasor, J. Gamache, and F. Marks, 2012: Multiscale analysis of tropical cyclone kinematic structure from airborne Doppler radar composites. *Mon. Wea. Rev.,* **140,** 77-99.

Rotunno, R., and J. B. Klemp, 1982: The influence of the shear-induced pressure gradient on thunderstorm motion. *Mon. Wea. Rev.,* **110,** 136-151.

Saffir, H. S., 2003: Communicating damage potentials and minimizing hurricane damage, *Hurricane! Coping With Disaster,* edited by R. Simpson, pp. 155-164, AGU, Washington, D.C.

Samsury, C. E., and E. J. Zipser, 1995: Secondary wind maxima in hurricanes: Airflow and relationship to rainband. *Mon. Wea. Rev.,* **123,** 3502-3517.

Schubert, W. H., and J. J. Hack, 1982: Inertial stability and tropical cyclone development. *J. Atmos. Sci.,* **39,** 1687-1697.

Schwendike, J., and J. D. Kepert, 2008: The boundary layer winds in Hurricanes Danielle (1998) and Isabel (2003). *Mon. Wea. Rev.,* **136**, 3168-3192.

Shapiro, L. J., and H. E. Willoughby, 1982: The response of balanced hurricanes to local sources of heat and momentum. *J. Atmos. Sci.,* **39,** 378-394.

Steiner, M., R. A. Houze Jr., and S. E. Yuter, 1995: Climatological characterization of three-dimensional storm structure from operational radar and rain gauge data. *J. Appl. Meteor.,* **34,** 1978-2007.

Terwey, W. D., and M. T. Montgomery, 2008: Secondary eyewall formation in two idealized, full-physics modeled hurricanes. *J. Geophys. Res.,* **113,** D12112, doi :10.1029/2007JD008897.

Testud, J., P. H. Hildebrand, and W.-C. Lee, 1995: A procedure to correct airborne Doppler radar data for navigation errors using the echo returned from the earth's surface. *J. Atmos. Oceanic Technol.,* **12,** 800-820.

Willoughby, H. E., F. D. Marks Jr., and R. J. Feinberg, 1984: Stationary and moving convective bands in hurricanes. *J. Atmos. Sci.,* **41,** 3189-3211.

Yano, J.-I., and K. A. Emanuel, 1991: An improved WISHE model of the equatorial atmosphere and its coupling with the stratosphere. *J. Atmos. Sci.*, **48,** 377-389.

Yuter, S. E., and R. A. Houze Jr., 1997: Measurements of raindrop size distributions over the Pacific warm pool and implications for Z-R relations. *J. Appl. Meteor.*, **36,** 847-867.

Zhang, J. A., R. F. Rogers, D. S. Nolan, and F. D. Marks Jr., 2011: On the characteristic height scales of the hurricane boundary layer. *Mon. Wea. Rev.*, **139**, 2523-2535.

Zipser, E. J., 2003: Some views on "hot towers" after 50 years of tropical field programs and two years of TRMM data. *Cloud Systems, Hurricanes, and the Tropical Rainfall Measuring Mission (TRMM), Meteor. Monogr.,* No. 51, Amer. Meteor. Soc., 49-58.

Figure Captions

Figure 1. Plan view of ELDORA reflectivity data at 2-km altitude observed during 1845-1927 UTC 21 Sep 2005. Visible satellite imagery from *GOES-E* is shown in the background. Boxes outline sections A-D used in the analysis.

Figure 2. Results of convective-stratiform separation algorithm applied to ELDORA reflectivity data shown in Fig. 1. Red indicates convective regions, orange indicates stratiform regions, and green indicates weak-echo regions. The overlying black circle encompasses the eyewall convection and the black spiral divides the "inner" convection from the "outer" convection.

Figure 3. a) Composite of radial velocity from radially aligned cross sections of convective cells in the inner upwind region. Average reflectivity values are overlaid as black contours (dBZ). b) As in (a), but for tangential velocity. Positive values are cyclonic. c) As in (a), but for vertical velocity. d) As in (a), but for divergence. Selected streamlines of the radial and vertical velocities are drawn.

Figure 4. Same as Fig. 3, but for cross sections of convective cells in the outer upwind region.

Figure 5. a) Magnitude and altitude of maximum averaged tangential wind for each cross section in the inner and outer upwind regions. Tangential velocities are averaged over the horizontal distance 14-20 km from Figs. 3 and 4. b) Frequency of tangential maxima occurring at each altitude normalized by total for each region.

Figure 6. Vertical profiles of the mean vertical velocity for pixels classified as convective in the upwind inner region (solid) and the upwind outer region (dashed). Profiles displayed are updrafts, downdrafts, and total vertical velocity.

Figure 7. a) Vertical profiles of the mean radial velocity for pixels classified as convective in the inner and outer upwind regions. b) As in (a), but for the mean tangential velocity.

Figure 8. a) Vertical profiles of radial momentum budget terms from Eq. (1), averaged over pixels classified as convective in the upwind inner region. b) As in (a), but for the upwind outer region.

Figure 9. Summed vertical profiles of the mean radial momentum budget terms from the convective pixels in the upwind inner and outer regions.

Figure 10. Composite of GBR values from radially aligned cross sections of convective cells in the inner upwind region. Average reflectivity values are overlaid as black contours (dBZ).

Figure 11. Same as Fig. 8, but for tangential momentum budget terms from Eq. (4).

Figure 12. Same as Fig. 9, but for tangential momentum budget terms.

Figure 13. Azimuthally averaged field of radial velocity from sections A and B. Average reflectivity values are overlaid as black contours (dBZ).

Figure 14. Vertical profiles of the mean radial velocity in the inner and outer regions for sections A-D.

Figure 15. Same as Fig. 14, but for vertical profiles of the mean tangential velocity.

Figure 16. Plan view of ELDORA reflectivity data at 2-km altitude observed during 2010-2032 UTC. The section outlined in black shows the region analyzed in Fig. 17.

Figure 17. a) Averaged vertical cross section of radial velocity from outlined section in Fig. 16. Reflectivity values are overlaid as black contours (dBZ). Cell A and Cell B are indicated. b) As in (a), but for tangential velocity. c) As in (a), but for radial component of divergence. d) As in (a), but for total horizontal divergence.

Figure 18. Schematic of the convective motions associated with two mature convective cells at different radial distances from the storm center within the inner core. Reflectivity contours are drawn showing Cell 1 at a smaller radius and Cell 2 and a larger radius. The solid arrows represent the overturning secondary circulation within each cell. The plus signs and minus signs indicate regions of increasing and decreasing tangential velocity, respectively. V_1 and V_2 represent the tangential velocity jets in each cell.

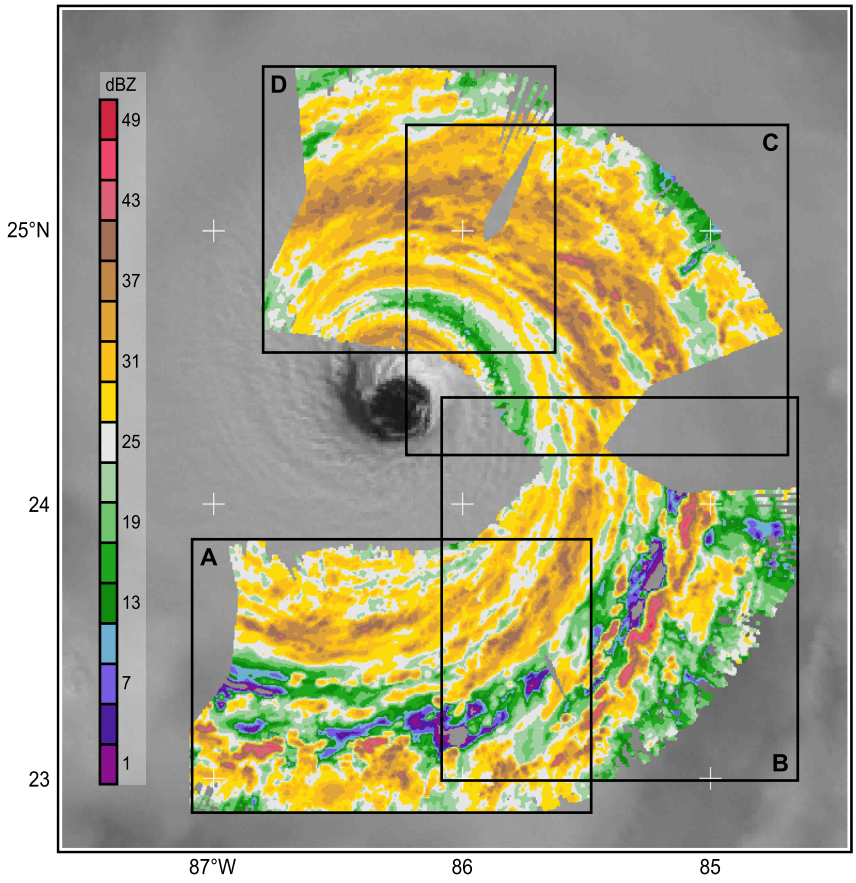

Figure 1. Plan view of ELDORA reflectivity data at 2-km altitude observed during 1845-1927 UTC 21 Sep 2005. Visible satellite imagery from *GOES-E* is shown in the background. Boxes outline sections A-D used in the analysis.

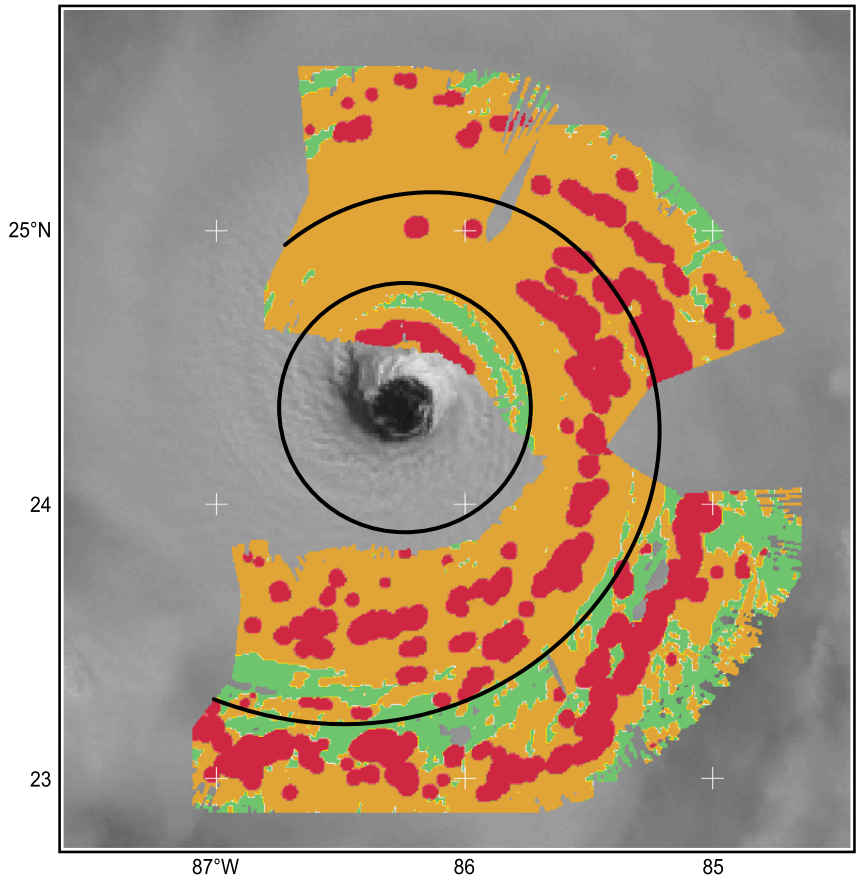

Figure 2. Results of convective-stratiform separation algorithm applied to ELDORA reflectivity data shown in Fig. 1. Red indicates convective regions, orange indicates stratiform regions, and green indicates weak-echo regions. The overlying black circle encompasses the eyewall convection and the black spiral divides the "inner" convection from the "outer" convection.

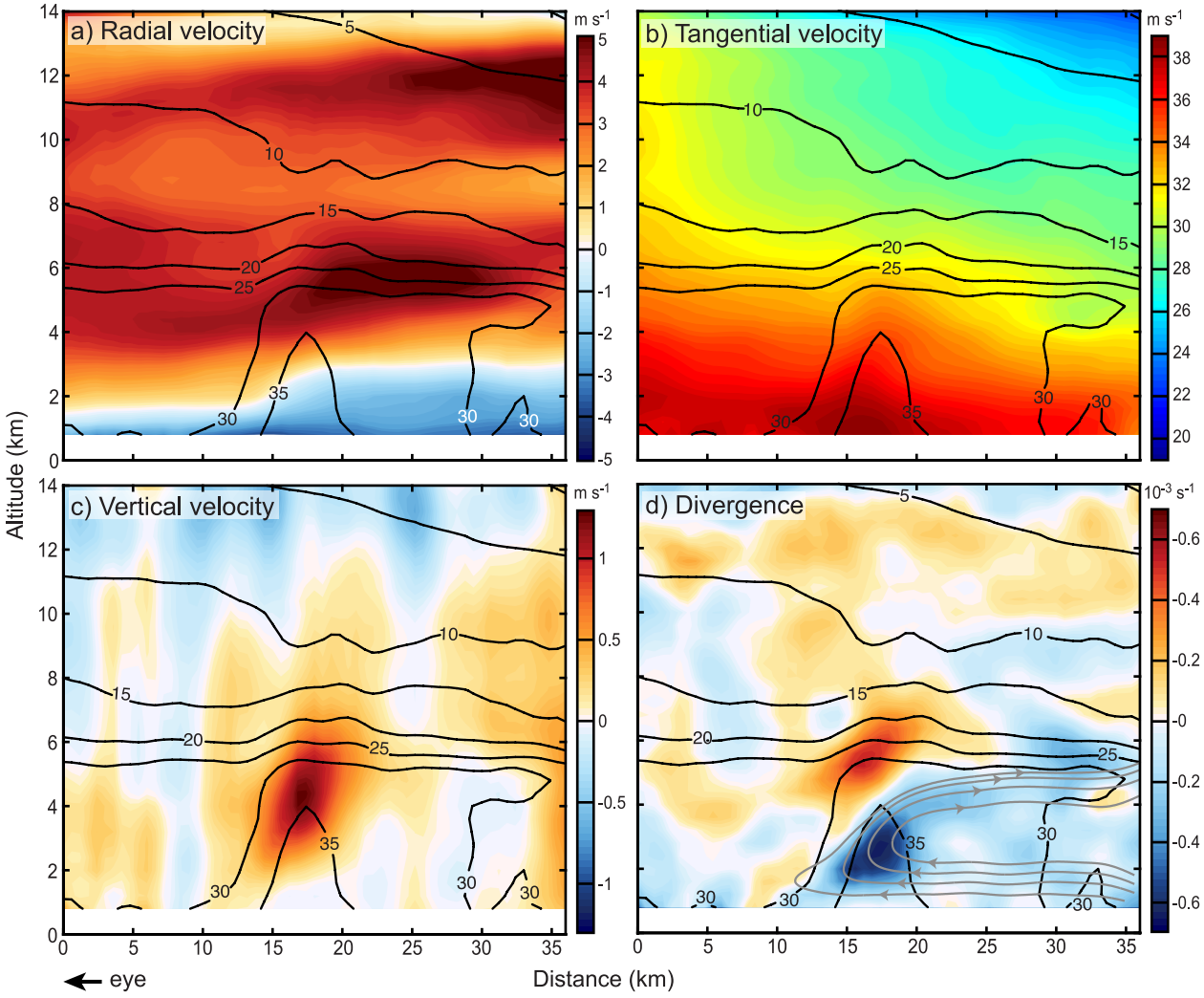

Figure 3. a) Composite of radial velocity from radially aligned cross sections of convective cells in the inner upwind region. Average reflectivity values are overlaid as black contours (dBZ). b) As in (a), but for tangential velocity. Positive values are cyclonic. c) As in (a), but for vertical velocity. d) As in (a), but for divergence. Selected streamlines of the radial and vertical velocities are drawn.

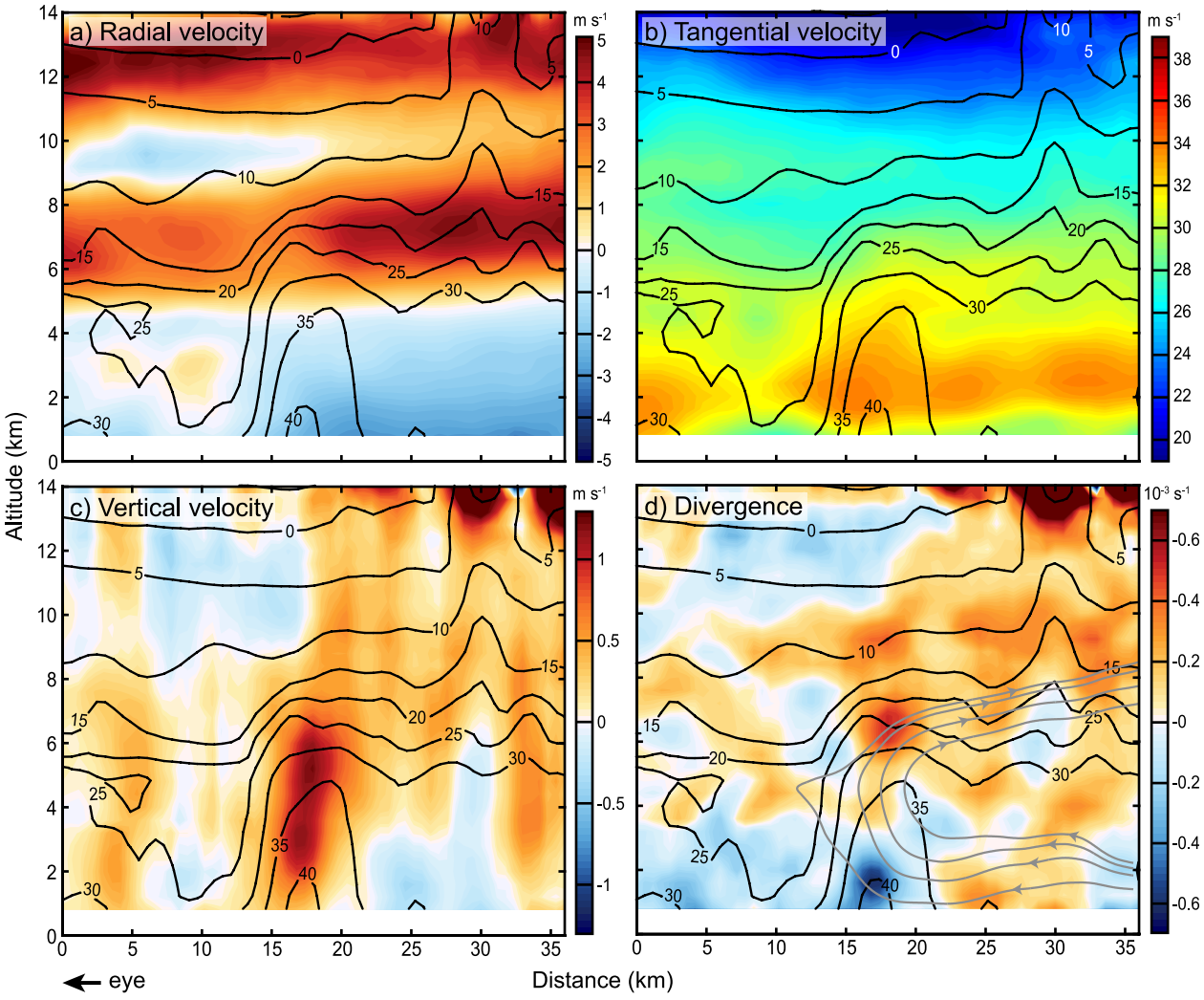

Figure 4. Same as Fig. 3, but for cross sections of convective cells in the outer upwind region.

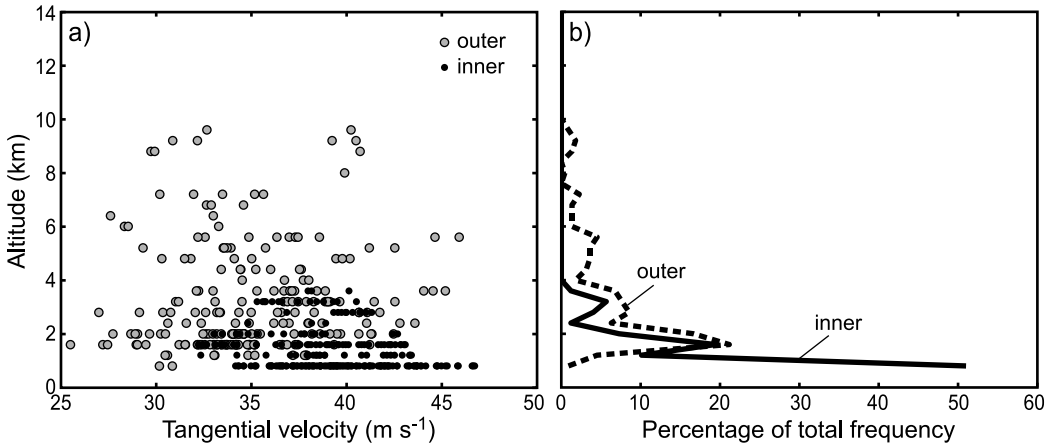

Figure 5. a) Magnitude and altitude of maximum averaged tangential wind for each cross section in the inner and outer upwind regions. Tangential velocities are averaged over the horizontal distance 14-20 km from Figs. 3 and 4. b) Frequency of tangential maxima occurring at each altitude normalized by total for each region.

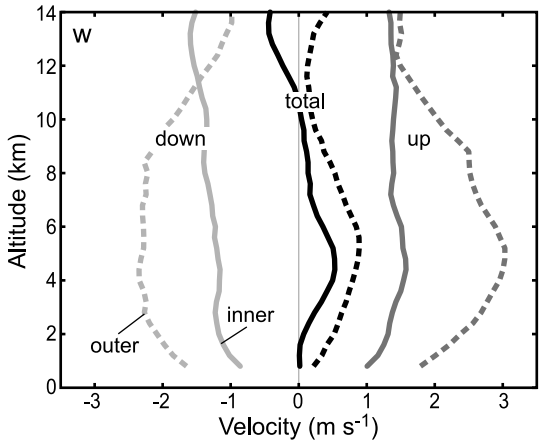

Figure 6. Vertical profiles of the mean vertical velocity for pixels classified as convective in the upwind inner region (solid) and the upwind outer region (dashed). Profiles displayed are updrafts, downdrafts, and total vertical velocity.

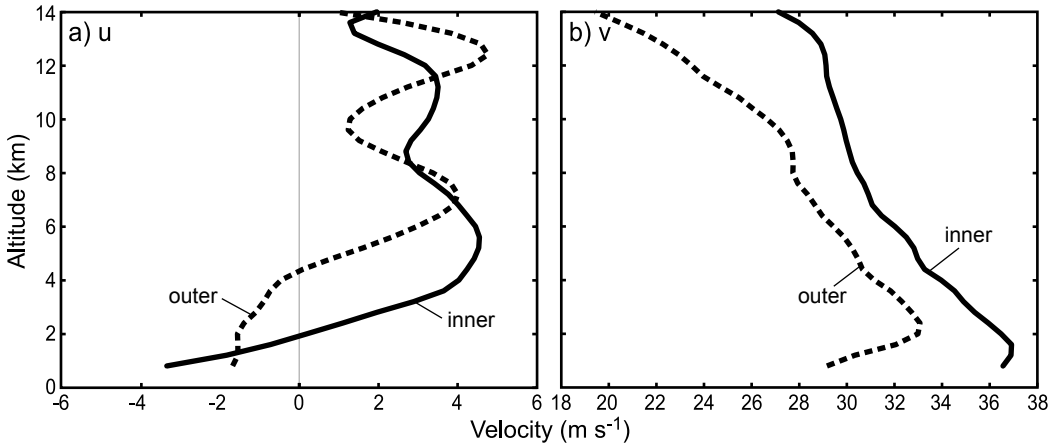

Figure 7. a) Vertical profiles of the mean radial velocity for pixels classified as convective in the inner and outer upwind regions. b) As in (a), but for the mean tangential velocity.

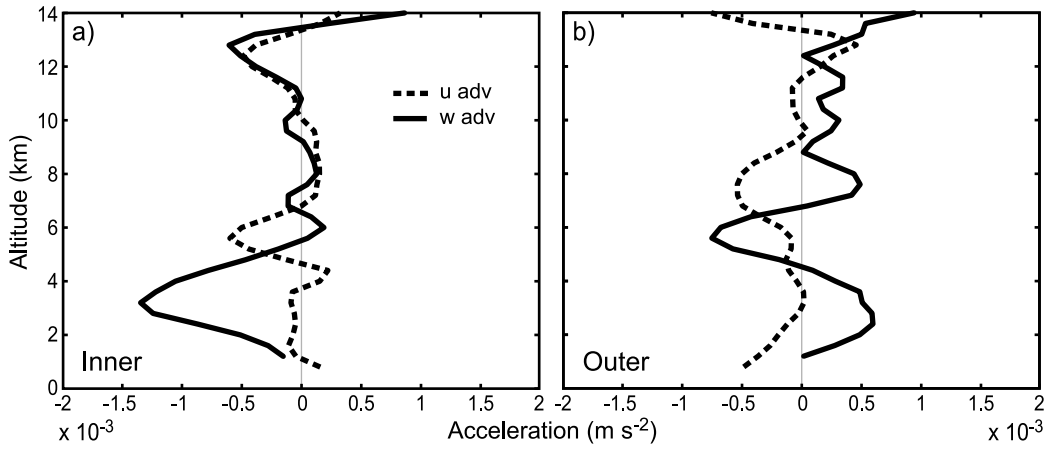

Figure 8. a) Vertical profiles of radial momentum budget terms from Eq. (1), averaged over pixels classified as convective in the upwind inner region. b) As in (a), but for the upwind outer region.

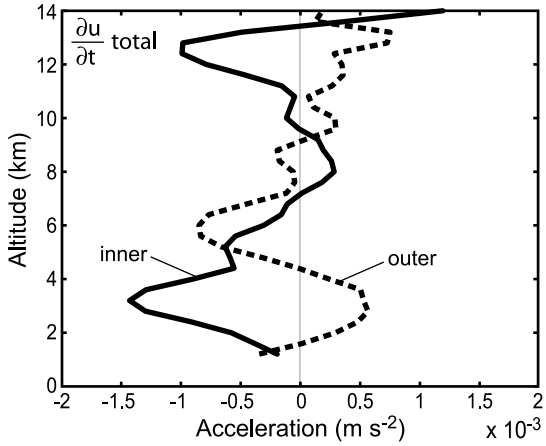

Figure 9. Summed vertical profiles of the mean radial momentum budget terms from the convective pixels in the upwind inner and outer regions.

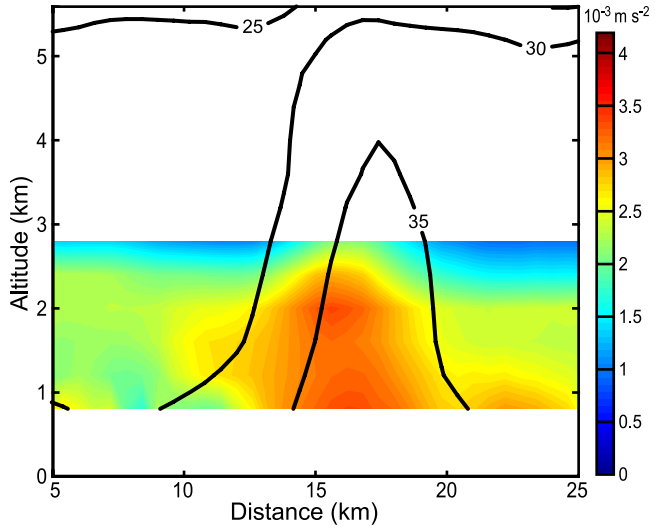

Figure 10. Composite of GBR values from radially aligned cross sections of convective cells in the inner upwind region. Average reflectivity values are overlaid as black contours (dBZ).

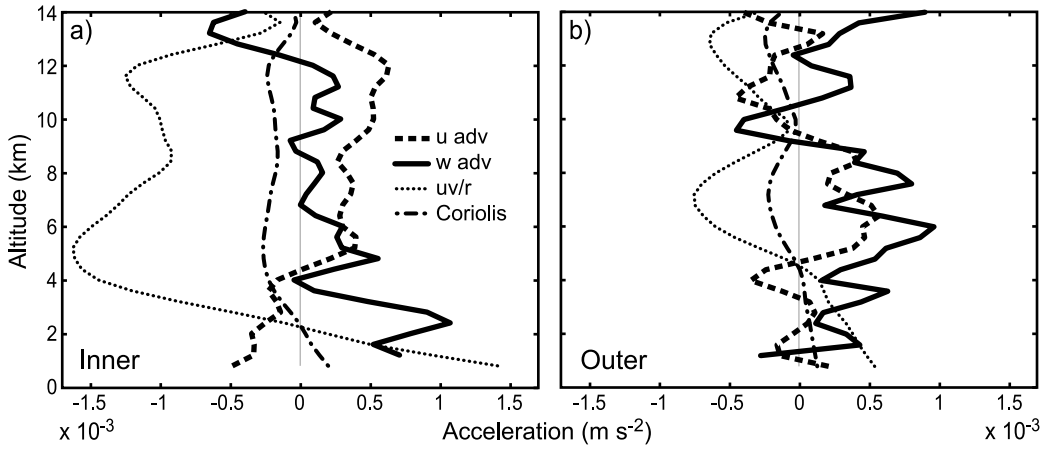

Figure 11. Same as Fig. 8, but for tangential momentum budget terms from Eq. (4).

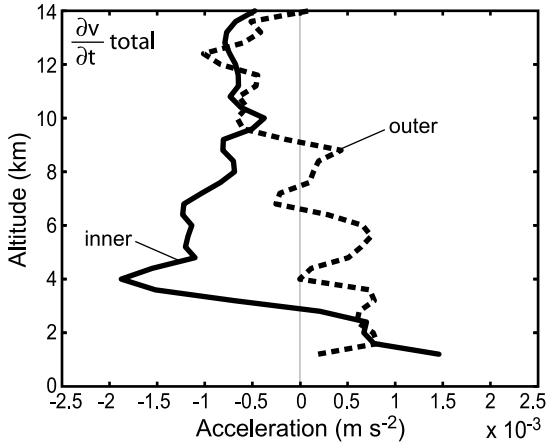

Figure 12. Same as Fig. 9, but for tangential momentum budget terms.

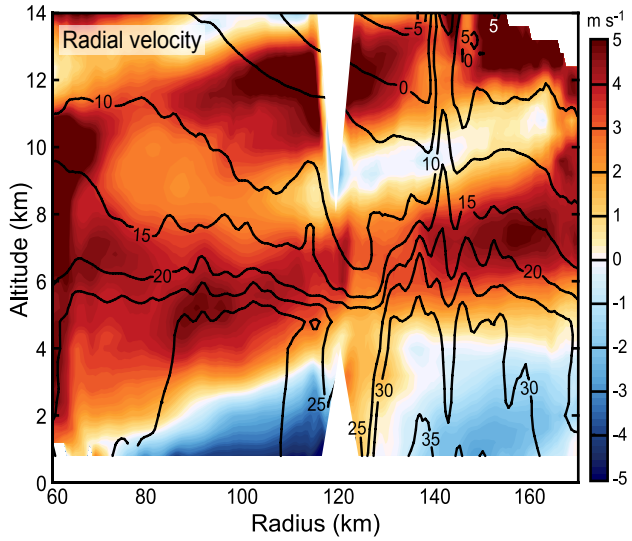

Figure 13. Azimuthally averaged field of radial velocity from sections A and B. Average reflectivity values are overlaid as black contours (dBZ).

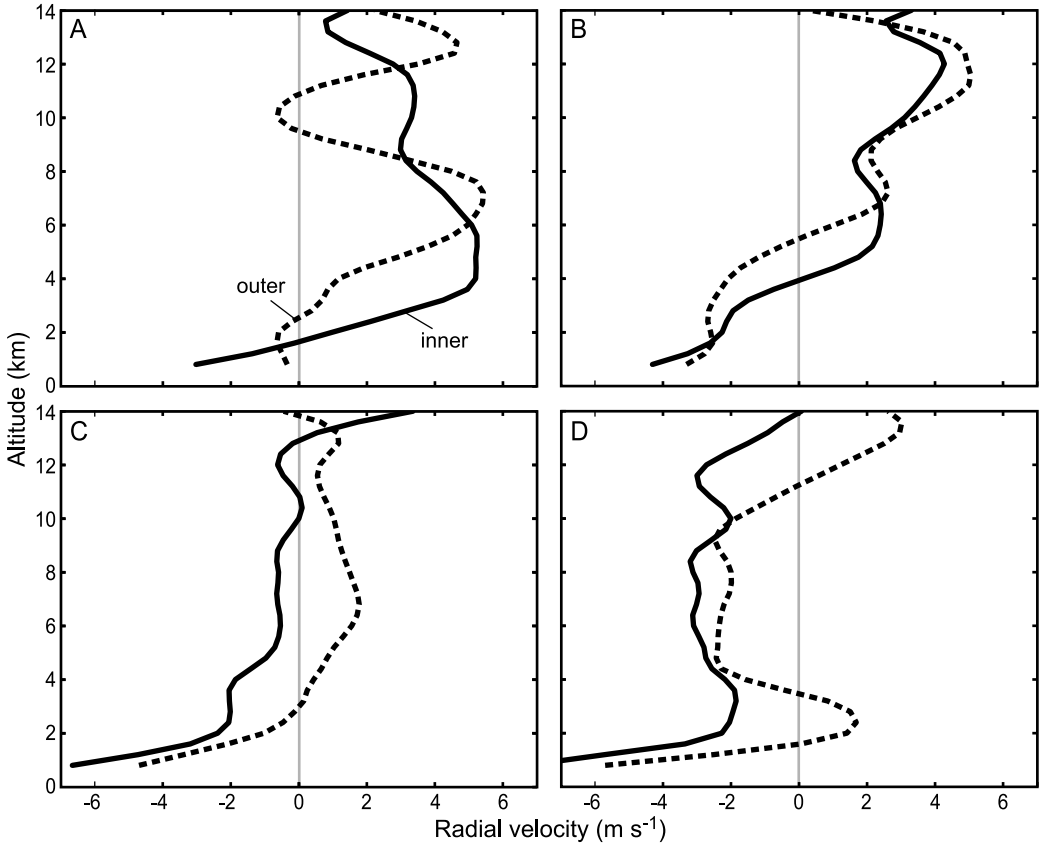

Figure 14. Vertical profiles of the mean radial velocity in the inner and outer regions for sections A-D.

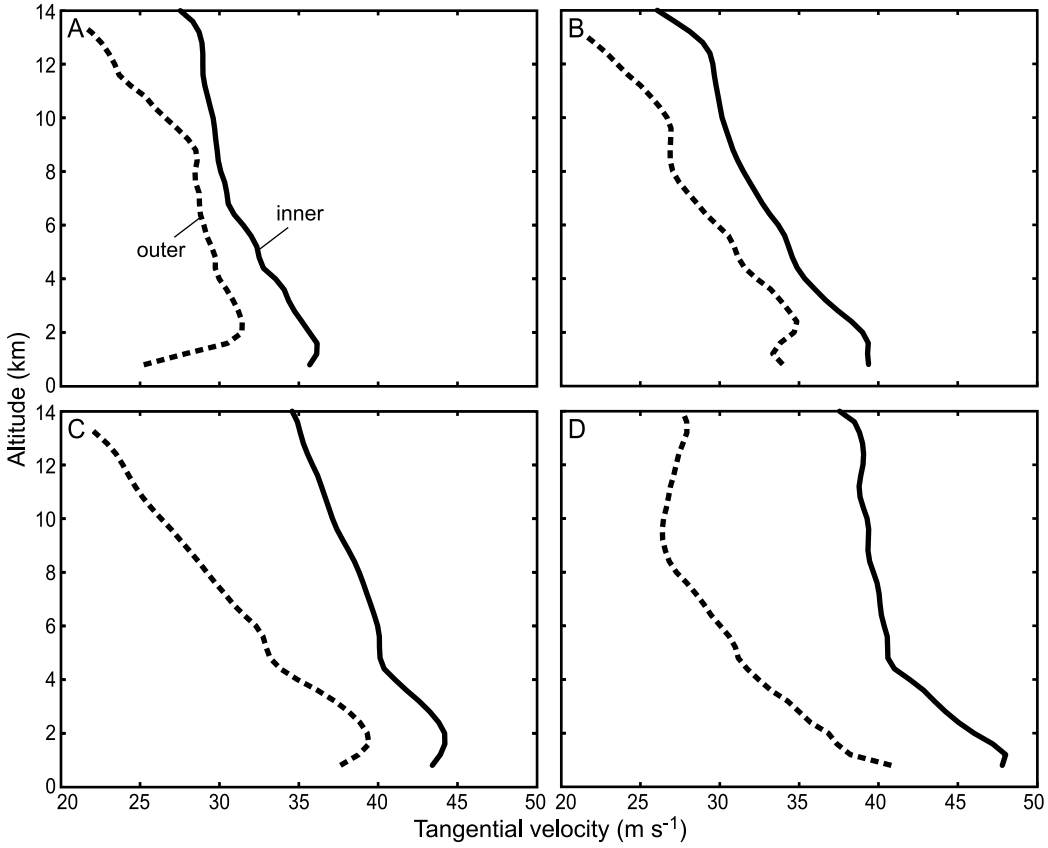

Figure 15. Same as Fig. 14, but for vertical profiles of the mean tangential velocity.

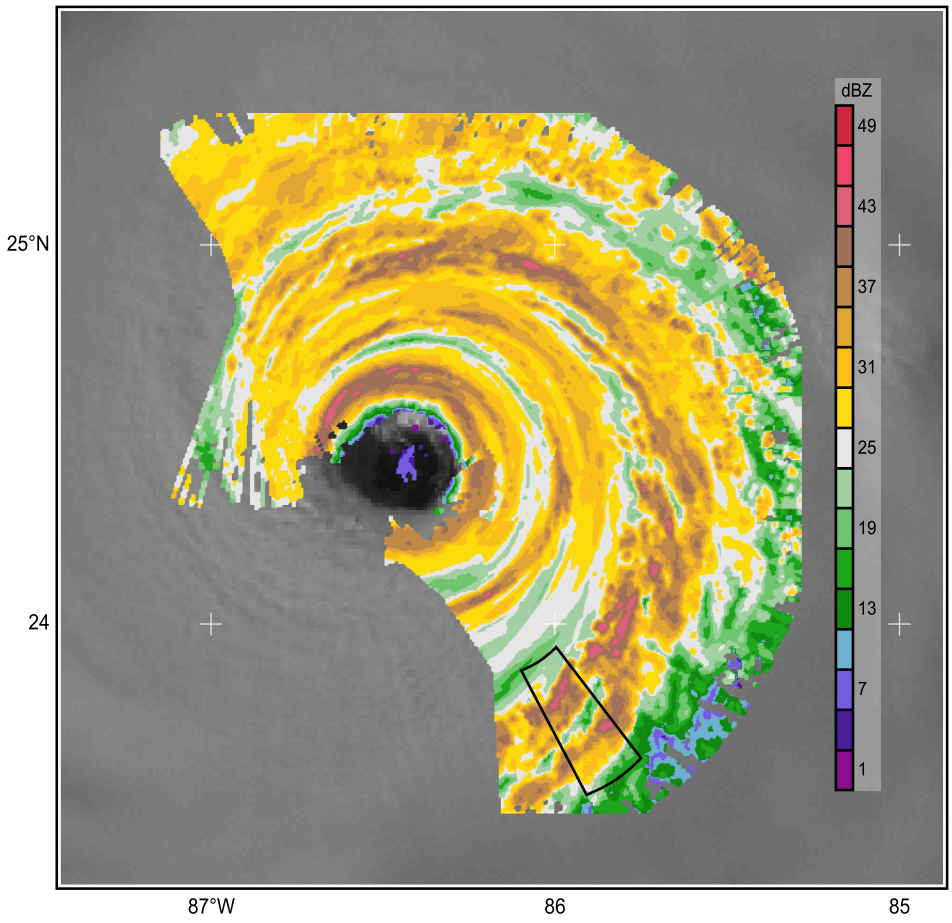

Figure 16. Plan view of ELDORA reflectivity data at 2-km altitude observed during 2010-2032 UTC. The section outlined in black shows the region analyzed in Fig. 17.

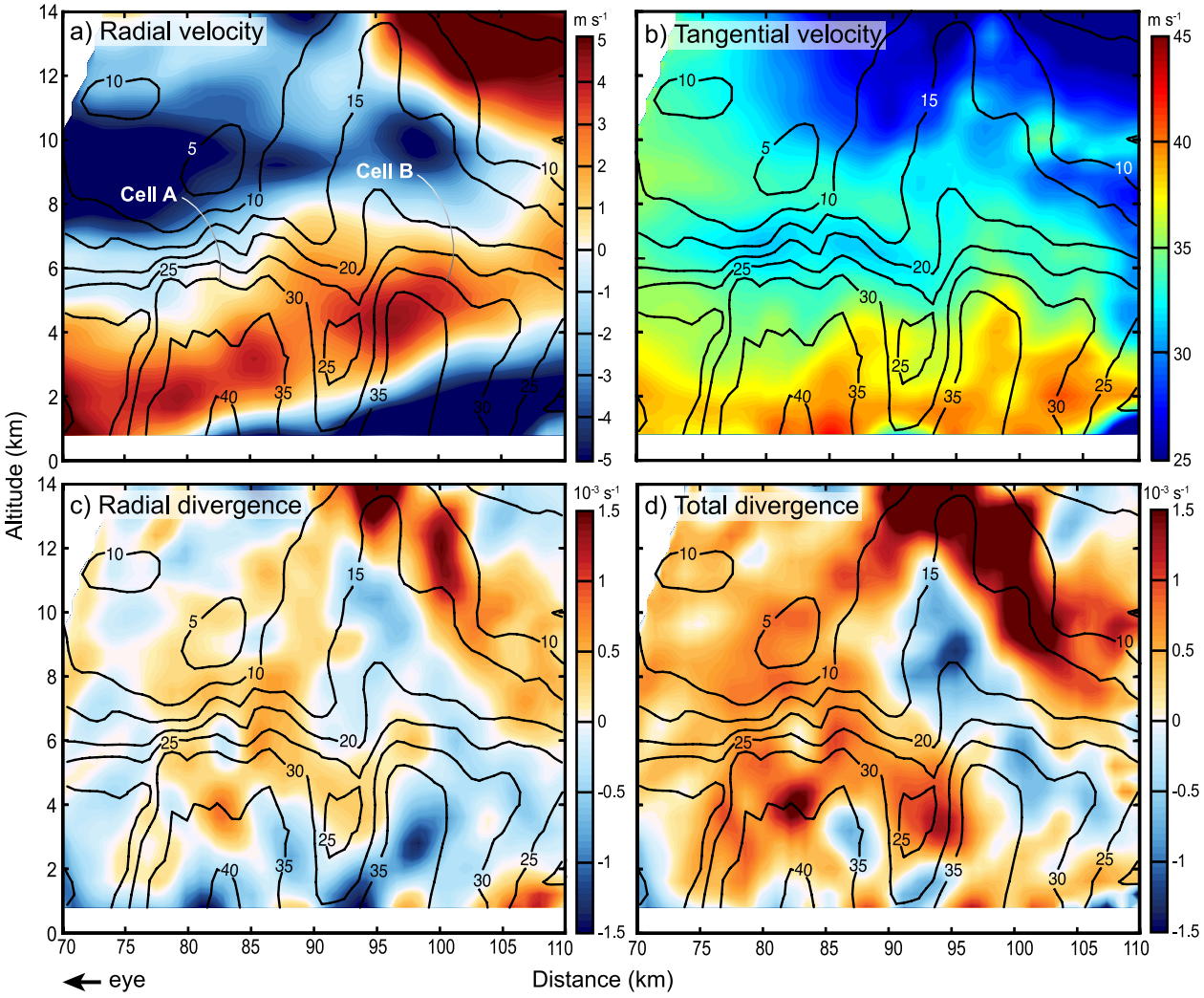

Figure 17. a) Averaged vertical cross section of radial velocity from outlined section in Fig. 16. Reflectivity values are overlaid as black contours (dBZ). Cell A and Cell B are indicated. b) As in (a), but for tangential velocity. c) As in (a), but for radial component of divergence. d) As in (a), but for total horizontal divergence.

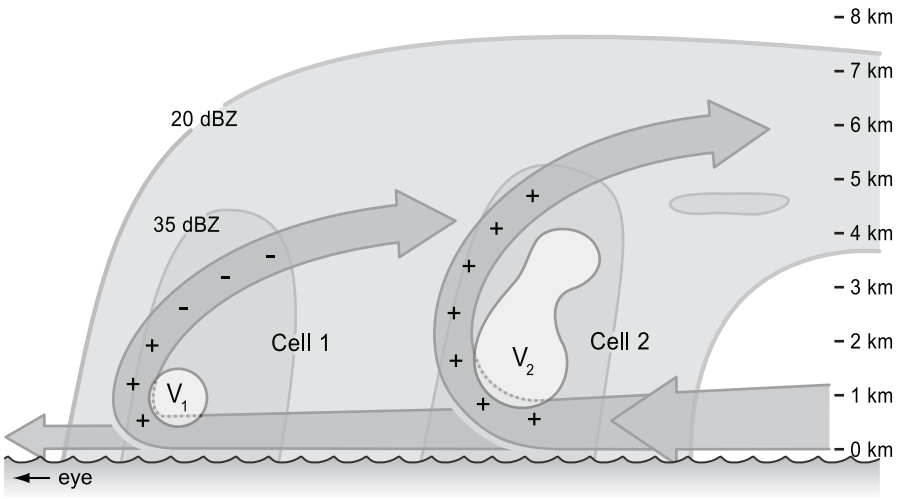

Figure 18. Schematic of the convective motions associated with two mature convective cells at different radial distances from the storm center within the inner core. Reflectivity contours are drawn showing Cell 1 at a smaller radius and Cell 2 and a larger radius. The solid arrows represent the overturning secondary circulation within each cell. The plus signs and minus signs indicate regions of increasing and decreasing tangential velocity, respectively. V_1 and V_2 represent the tangential velocity jets in each cell.